


Highly active air electrode catalysts for Zn-air batteries: Catalytic mechanism and active center from obfuscation to clearness

Wenhui Deng¹ | Zirui Song² | Mingjun Jing³ | Tianjing Wu³  |
Wenzhang Li¹ | Guoqiang Zou¹

¹College of Chemistry and Chemical Engineering, Central South University, Changsha, China

²Department of Materials, University of Oxford, Oxford, UK

³National Local Joint Engineering Laboratory for Key Materials of New Energy Storage Battery, Key Laboratory of Environmentally Friendly Chemistry and Application of Ministry of Education School of Chemistry, Hunan Province Key Laboratory of Electrochemical Energy Storage & Conversion, National Base for International Science & Technology Cooperation, School of Chemistry Xiangtan University, Xiangtan, China

Correspondence

Tianjing Wu, National Local Joint Engineering Laboratory for Key Materials of New Energy Storage Battery, Key Laboratory of Environmentally Friendly Chemistry and Application of Ministry of Education School of Chemistry, Hunan Province Key Laboratory of Electrochemical Energy Storage & Conversion, National Base for International Science & Technology Cooperation, School of Chemistry Xiangtan University, Xiangtan 411105, China.
Email: twu@xtu.edu.cn

Wenzhang Li and Guoqiang Zou, College of Chemistry and Chemical Engineering, Central South University, Changsha 410083, China.
Email: liwenzhang@csu.edu.cn and gq-zou@csu.edu.cn

Funding information

Distinguished Young Scholar Fund Project of Hunan Province Natural Science Foundation, Grant/Award Number: 2023JJ10041; Science and Technology Program of Xiangtan, Grant/Award Numbers: GX-ZD20211004, GX-ZD20221007; Hunan Provincial Education Office Foundation of China, Grant/Award Number: 22A0114; National Natural Science Foundation of China,

Abstract

Carbon-based materials have been found to accelerate the sluggish kinetic reaction and are largely subject to the overall Zn-air batteries (ZABs) property, while their full catalytic mechanism is still not excavated because of the indistinct internal structure and immature in-situ technology. Up to now, systematic methods have been utilized to study and design promising high-performance carbon-based catalysts. To resolve the real active units and catalytic mechanism, developing molecular catalyst is a significant strategy. Herein, the review will initiate to briefly introduce the working principle and composition of ZABs. An important statement is correspondingly provided about the typical structure and catalytic mechanisms for the air cathode material. It also presents the tremendous endeavors on the catalytic performance and stability of carbon-based material. Furthermore, combined with theoretical calculation, the self-defined active sites are analyzed to understand the catalytic character, where the molecular catalyst is subsequently summarized and discussed through highlighting the unambiguous and controllable structure, in the hope of surfacing the optimum catalyst. Building on the fundamental understanding of carbon-based and molecular catalysts, this review is expected to provide guidance and direction toward designing future mechanistic studies and ORR electrocatalysts.

This is an open access article under the terms of the [Creative Commons Attribution](https://creativecommons.org/licenses/by/4.0/) License, which permits use, distribution and reproduction in any medium, provided the original work is properly cited.

© 2024 The Authors. *Carbon Neutralization* published by Wenzhou University and John Wiley & Sons Australia, Ltd.

KEYWORDS

air electrode, catalytic mechanism, electrolyte, molecular catalysts, Zn anode

1 | INTRODUCTION

The global greenhouse effect has intensified due to the uncontrolled use and emissions of nonrenewable energy, leading to the frequent occurrence of various climate disasters. Addressing global climate change, renewable energy sources is the only way for a sustainable economy.^[1–3] All clean electricity (renewables and nuclear) together accounts for 39% of global electricity while fossil fuels still generated 61% in 2022. Therefore, renewable energy sources are to replace fossil power, which is considered a promising strategy. Renewable energy sources are confronted with drawbacks such as high difficulty in prediction, regional limitations, and unstable production capacity. It is necessary to design a high energy density and safe energy storage system. At present, lithium-ion batteries (LIBs) are widely deemed as the most feasible options for energy equipment owing to their outstanding energy density (up to 750 Wh l^{−1}).^[4] Although advantages are so attractive, LIBs are currently suffering from the high cost of Li-metal and potential safety problems. To overcome these issues, aqueous metal-air batteries received a large amount of attention over recent years. Among them, Zn-air batteries (ZABs) are considered the highly promising energy storage system, owing to their inexpensive, hazard-free, and high theoretical energy density of (1086 Wh kg^{−1}).^[5] Nevertheless, sluggish kinetics and overpotential of oxygen reduction/evolution reaction (ORR/OER) hinder their further applications. To overcome these problems, developing highly efficient bifunctional oxygen materials is critical to obtaining the practical application.

According to the volcanic type diagram, various catalysts have different adsorption capacities for the intermediate species of ORR. Pt-based catalysts exhibit ideal reactivity due to the moderate absorption ability of reactive intermediate. Unfortunately, the high price and low stability limit their applications.^[6] To obtain more efficient catalysts, substantial efforts have been carried out in carbon-based materials. The carbon-based metal-free material (CB-MFM) materials have been broadly studied owing to their diverse structures and low cost.^[7] The CB-MFM activity is gradually improving through rational design and synthesis. Initially, the pristine carbon material (graphene, carbon nanocage, and carbon black) possesses a uniform electronic structure, which is too inert as the active site of ORR.^[8] In the last decade, the catalytic activities of CB-MFM received efficient

improvement through heteroatom doping, defective introduction, and surface modification. Among them, heteroatom doping carbon material can change the charge density and distribution due to the difference between heteroatom and carbon atoms in atomic radius and electronegativity.^[9] Moreover, doping can also introduce the defect structure in the carbon skeleton to further improve electrocatalytic activity.^[10] For example, in 2009, the first discovery of CB-MFM (vertically aligned N-doped carbon nanotubes) possessed an excellent ORR performance in alkaline solution.^[11] Although the ORR performance is gradually rising, the doping effect and structural diversity for CB-MFM have still insufficient understanding. Moreover, the oxygen adsorption-desorption process and OER reaction mechanism are also not clear. Compared to CB-MFM, the carbon-based transition metal catalysts (CB-TMC) have significantly improved the electrocatalytic activity and stability, making a new level.^[12] In general, the pyrolysis has been widely used to synthesize CB-TMC. In the pyrolysis process, the metal atoms tend to agglomerate because the free energy of the metal surface is reduced and thermodynamic instability. The metal agglomerate may cause many negative factors, which produce a mass of the inactive structure, reduce the efficient utilization of metal atoms, and become blurry and complex for simple catalytic system. However, these catalysts have occurred in the complex ORR reaction pathway. Pyrolysis of multiple precursors can generate a highly heterogeneous and complex structure. Meanwhile, the pyrolysis process is very energy-intensive. New insights about the catalytic nature of catalysts have been proposed through advanced characterization techniques. To understand the catalytic principles, the rational design and synthesis of CB-TMC appear particularly important. When the nanoparticle catalysts are downsizing to atomic levels, some unique physical and chemical properties will emerge.^[13–15] Moreover, single atomic catalysts (SACs) possess a high atom-utilization ratio and outstanding activity.^[16–18] Although the SACs can display activity and stability approaching the noble-metal catalysts, the original structure of catalysts can be destroyed in the synthesis process. Thus, elucidating the structure-function relationship cannot be fundamentally solved. Meanwhile, the potential synergistic effect can also negative factor for the catalytic activity. Therefore, the noncarbonized synthesis strategies significantly solve the aforementioned issues. The pyrolysis-free route can precisely

design and fabricate the definite molecular structure, which is the critical step in analyzing the catalytic mechanism.^[19–21] The definite active units are of great importance for the guidance of optimum electrocatalysts.

The review summarizes various carbon-based and molecular catalysts to apply in ZABs. The catalytic performance of carbon-based material will arrive peak. However, the catalytic mechanisms are still widely differing versions. The structure-performance relationships feel at a loss. Identification of active centers is objective. The pivotal performance optimization strategies have no way to start. Therefore, a definite catalytic system appears particularly important to demonstrate in-depth mechanism understanding and rational design for the optimal catalyst. In this review, the working fundamentals and constitution of overall ZABs are briefly introduced. Then, a distinct statement is provided about the typical structure and catalytic performance relationship. In previous decades, science researchers made a tremendous effort in performance modification (heteroatom doping, defect structure, and metal atom modification). Numerous carbon-based catalysts have possessed outstanding electrocatalytic properties than those of noble-based catalysts. Although the performance has made significant improvements, the catalytic mechanism is equally important and challenging. To further boost the catalytic activity, the structural clarity is particularly important. The distinct molecular catalyst can make a huge contribution to the understanding of reaction mechanisms and structure-performance relationships. Finally, the review will propose deep insights into the future of catalysts.

2 | MECHANISMS AND CONFIGURATIONS OF ZABs

2.1 | Working principle of ZABs

The typical ZABs are made up of Zn flakes/particles anode, air cathode, and alkaline electrolyte (KOH or NaOH) as well as membrane separator. ZABs can be divided into disposable or reversible ZABs. The working life of the disposable ZABs is closely connected to the zinc electrode. After the Zn electrode (zinc sheet or zinc paste) is used up, the battery cannot be used again. However, the reversible ZABs can be recharged when the electricity is completely consumed. The air cathode absorbs active substances (oxygen) from the air. The electrolyte is generally 6 M KOH + 0.2 M Zn(CH₃COO)₂ aqueous electrolyte. In Figure 1, the internal reaction principle of ZABs is similar to that of an ordinary alkaline battery, and its basic working principle can be summarized as follows: the zinc electrode reacts with OH[−] during the

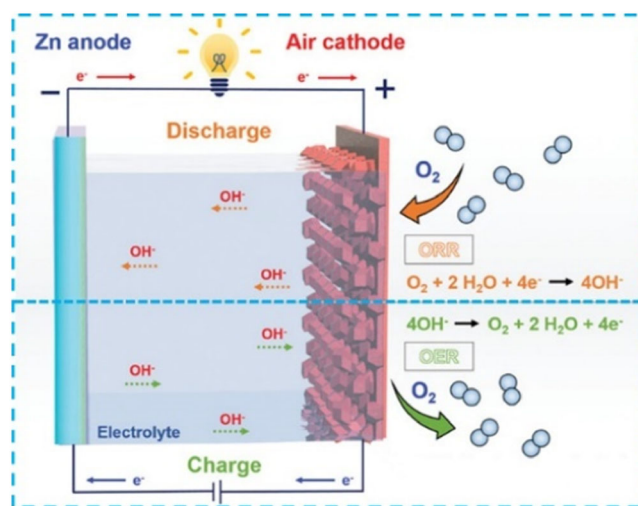
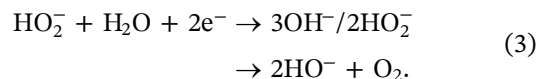
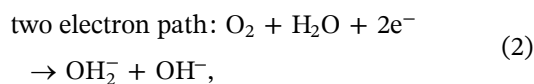
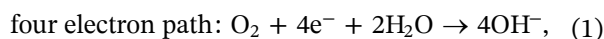


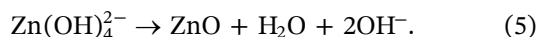
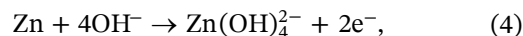
FIGURE 1 Zn-air batteries assembly and reaction mechanism. Reproduced with permission: Copyright 2021, Wiley-VCH.^[22]

discharge process. At the same time, oxygen is dissolved in the electrolyte and diffused to the catalytic layer to form a three-phase interface, where oxygen is reduced to OH[−]. At present, researchers generally believe that the process of air electrode discharge can be divided into “two electrons” and “four electrons” reactions. The four-electron process is preferred because the two-electron process may produce some harmful substances (hydrogen peroxide) and show low energy efficiency. The charging process is the opposite reaction. The basic reaction equation is as follows:

Air electrode discharge process^[23,24]:



Zn electrode discharge process:

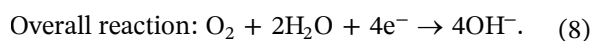


2.2 | Mechanism of ORR and OER

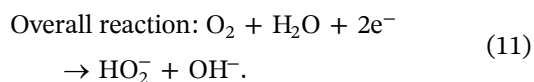
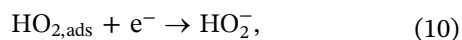
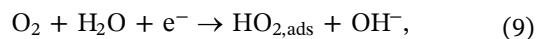
The ORR is the main reaction in a discharge process of ZABs, which is a typical multielectron reaction process with complex intermediate products.^[25] At present, researchers generally believe that the ORR process is

divided into “two-electron” and “four-electron” electrochemical reactions in an alkaline solution. The ORR pathway mainly relies on the following two types: one is bridge adsorption (two oxygen atoms are combined with metal atoms), and the other is end group adsorption (one oxygen atom is vertically combined with metal atoms), leading to $4e^-$ and $2e^-$ transfer process of oxygen reduction.

In alkaline electrolytes, bridging adsorption of oxygen molecules leads to the $4e^-$ transfer process as follows^[26,27]:



In alkaline electrolyte, the terminal group's adsorption of oxygen molecules leads to the $2e^-$ transfer process as follows:



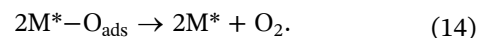
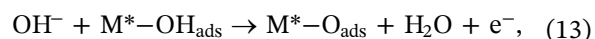
Where “ads” refers to the substances anchored in the catalyst external.

In the $2e^-$ transfer process, the production of peroxides are corrosive and poison the air electrode catalyst, resulting in the transitory cycle life of the ZABs.^[28] Therefore, the bridge-type oxygen adsorption

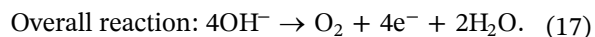
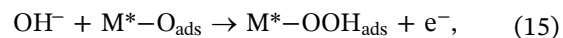
molecular path is the most suitable oxygen reduction reaction in the practical application of ZABs. In previous studies, a volcano plot was calculated and constructed through the different metal surfaces. As shown in Figure 2a, the precious metal Pt near the top is deemed to have good ORR properties. Nevertheless, the scarcity and poor stability of Pt-based catalysts impede its further application in reversible ZABs.

When the battery is charged, the OER is the reverse process. The OER is also a multielectron transfer, and the kinetic process is slow.

In an alkaline electrolyte, the mechanism of OER can be described by the following reaction^[29,30]:



Or:



M^* represents the active unit on the catalyst external.

The reaction equation shows that OH^- first reacts with the active centers of the catalyst to form M^*-OH_{ads} and an electron. Then it went through a complex reaction process. In the whole process of reaction, the

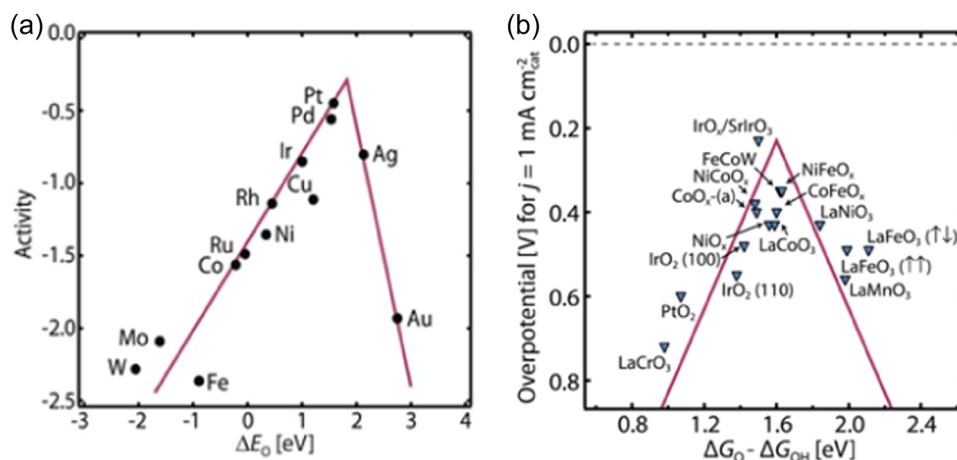


FIGURE 2 Volcano plot of ORR (a) and OER (b). Reproduced with permission: Copyright 2018, The American Association for the Advancement of Science.^[3]

adsorption/desorption of OH^- and O_2 will produce an electrode overpotential on the active site of the catalyst surface, resulting in a slow oxygen precipitation process. To speed up the kinetic process, it is necessary to lower the energy barrier of the OER and improve the catalytic activity.^[23] In Figure 2b, noble metal-based catalysts (IrO_2) exhibit excellent OER, but they are easy to be oxidized and dissolve in the electrolyte at high potential, resulting in reduced catalytic activity, high price, and single function effect.

2.3 | Zinc electrode

Zinc as the negative electrode has the properties of rich reserves, low toxicity, environmental friendliness, and relative stability in alkaline media. The zinc electrode is a crucial part of ZABs. A successful zinc electrode should possess a high content of utilizable active substance and exhibit excellent stability in charge and discharge cycles. During operation in a ZAB, the zinc electrode can experience four major phenomena (dendrite growth, hydrogen evolution corrosion, shape change, and passivation) to limit its performance (Figure 3a).^[31] In this section, these problems are discussed and analyzed in the following four sections.

2.3.1 | Dendrite growth

Zn dendrites are needle-like metal protrusions formed during the discharge/charge cycling process. The formation mechanism of Zn dendrites is widely studied in an aqueous solution. Zn electrode reaction in ZAB is mainly controlled by the liquid phase mass transfer process. The concentration of reactive active substances is very subtle on the near zinc electrode surface, forming a large concentration polarization phenomenon. The reactive active substances are more likely to diffuse the Zn electrode external bulge position causing the growth of original protrusions on the surface due to uneven current distribution.^[34] These protrusions are further consolidated and formed dendrites through the “top effect.” At low current density, the concentrated polarization can be alleviated. At high current density, the tree crystal problem is very serious. The performance and cycle life of the ZABs are affected by dendrite growth. Its formation may lead to serious problems including short circuits, shortened cycle life, reduced coulomb efficiency, and potential safety hazards.^[35] Therefore, restricting zinc dendrite formation is vitally important for the further advancement of ZABs.

At present, different approaches are attempted to mitigate zinc dendrite, including additives, alloys, cladding, and membranes. The additive makes the

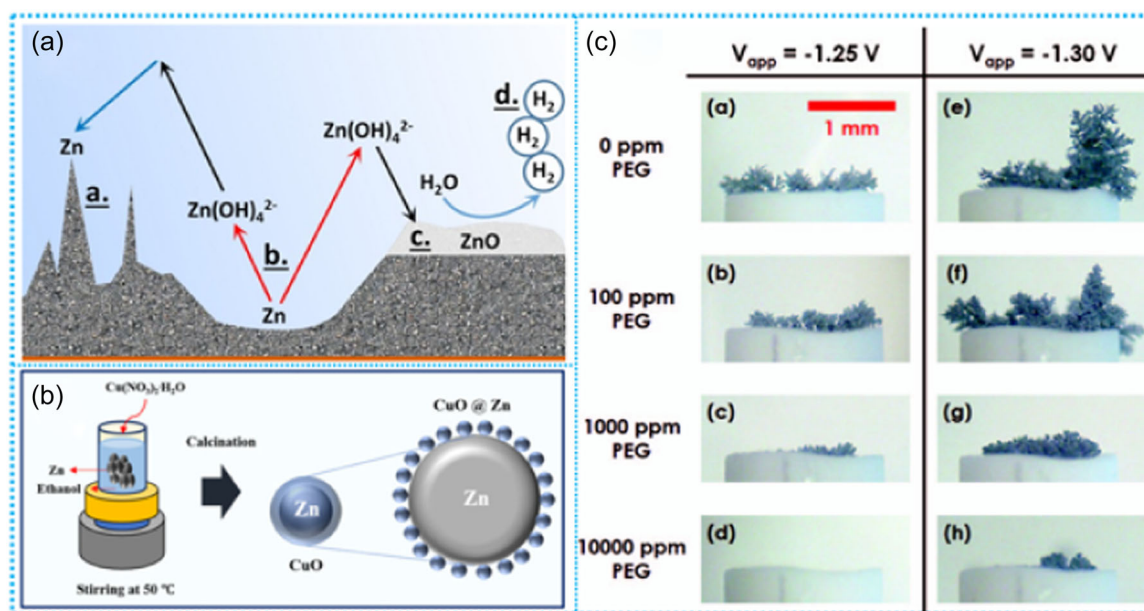


FIGURE 3 Schematic illustration of zinc electrode problems: (a) In aqueous solution system, a. dendrite growth, b. shape transformation, c. passivation, and d. H₂ evolution corrosion. Reproduced with permission: Copyright 2019, Elsevier Ltd.^[31] (b) Schematic illustration of the synthesis process of CuO@Zn electrode. Reproduced with permission: Copyright 2017, Wiley-VCH.^[32] (c) Optical microscopy of Zn dendrites growth in an alkaline electrolyte containing 0.1 M ZnCl₂ with different concentrations of PEG. Reproduced with permission: Copyright 2013, IOP science.^[33] The growth condition of zinc dendrite is exhibits at different electrode potentials. Moreover, Figure 3c including (a-h) demonstrate that PEG-200 as the additive can efficiently suppress the growth condition of zinc dendrite.

current evenly distributed on the electrode surface to inhibit the growth of dendrites. Moreover, the diaphragm inhibits dendrite growth through physical blocking. Banik and Akolkar^[33] studied the different contents of polyethylene glycol (PEG-200) could affect the formation rate of zinc dendrite through in-situ optical microscopy. As shown in Figure 3c, PEG-200 suppresses zinc dendrite growth in a wide range (100–10000 ppm) due to reducing the exchange current density of zinc electrodeposition. Meanwhile, the zinc dendrites formation was also affected by the concentration of PEG-200. A simple model for zinc dendrite growth was constructed and predicted dendrite growth rates, consistent with the experimental data. Peng et al.^[36] reported a novel Zn-Sn alloy as an anode electrode to control the dendrite formation and enhance the anticorrosion properties. The Zn-Sn alloy possessed even charge distribution on the surface and theoretical calculations also can testify to this result. The Zn-Sn alloy as ZABs anode exhibited a well-pleasing cycling life and rate property. Zhang et al.^[37] constructed a dense protective ZnSe layer in situ on the surface of a zinc anode (Zn@ZnSe). Bonding of Se atoms reduced the electron density around Zn atoms in the ZnSe layer and lessened the migration barrier on the surface, showing the low Zn affinity to increase the concentration of Zn^{2+} between the protective layer and the electrolyte cross-section. The homogenization of Zn^{2+} flux was promoted to eliminate interfacial side reactions and inhibit dendrite growth. Kim and Ryu^[32] observed that an appropriate copper oxide nanoparticle was modified zinc surface (CuO@Zn) which could validly prevent dendrite growth and improve the invertibility of the Zn electrode. Because of the isolation and minimum side effect of CuO, the CuO@Zn anode could enhance reversibility and cut down self-discharge (Figure 3b).

2.3.2 | Hydrogen evolutionary corrosion

The $\text{H}_2\text{O}/\text{H}_2$ reduction potential (-0.83 V vs. reversible hydrogen electrode [RHE]) is positive Zn/ZnO (-1.26 V vs. [RHE]) at pH 14. The zinc anode has thermodynamic properties and instability in an aqueous solution. Therefore, the H_2 evolution reaction (HER) is prone to happen, leading to surface corrosion. The HER can lead to the destruction of ZABs because of the increment of internal pressure and the consumption of the active substance.^[38] At present, strategies to inhibit the occurrence of zinc self-corrosion reactions have been extensively researched. The main measure is to add corrosion inhibitors in the electrode surface or inner, such as inorganic materials (metal and metal oxide) as well as an

organic protective film. For instance, Zhao et al.^[39] synthesized a coated zinc surface with a polyamide (PA) buffer layer. The PA buffer layer could improve the nucleation barrier of Zn^{2+} to regulate the deposition behavior of Zn^{2+} . Furthermore, it could inhibit corrosion and passivation. Lee et al.^[40] studied that the zinc particles combined with metal oxides (Bi_2O_3 , In_2O_3 , Al_2O_3) exhibited corrosion behavior in a 9 mol L^{-1} KOH electrolyte. The content of the hydrogen evolution-time curve displayed that mixing metal oxides in zinc particles could control the corrosion of zinc electrodes; among the three materials, Al_2O_3 represented the best corrosion inhibition effect. By measuring the constant current polarization, the corrosion current density of the Zn anode loaded with Al_2O_3 was smaller than the zinc electrode mixed with Al_2O_3 particles. Surface metalization was an effective method to reduce HER. The zinc electrode loaded with Al_2O_3 could prevent metal zinc from direct contact with KOH, thus playing the role of corrosion inhibition.

2.3.3 | Shape change

The shape change of Zn electrodes is also an important element affecting the capacity and cycling stability of ZABs. The shape change refers to the redistribution of Zn metal on the electrode surface after repeated charge/discharge cycles.^[41] In this reaction, the $\text{Zn}(\text{OH})_4^{2-}$ or Zn^{2+} dissolved in the charging process is redeposited in the different locations of the zinc plate, resulting in current concentration in specific areas during the discharge process. Nakata et al.^[42] used in situ XRD mapping measurement to elucidate the shape change of the Zn electrode. In charge, ZnO stayed in the heartland of the electrode. In discharge, ZnO grew vertically on the electrode, and along with zinc metal was oxidized and dissolved. Therefore, zinc deposition was not uniform, and zinc deposition sites were reduced to appear with a large amount of dead Zn.

Most researchers believe that the Zn electrode underwent shape transformation due to the concentration of zincate in alkaline electrolytes and the unevenness of current density distribution on the electrode surface. zhu et al.^[43] prepared neodymium hydroxides and lanthanum coating on zinc electrodes via the electrolysis method. The modification electrode could impede the movement of zinc species and minimize the dissolution of $\text{Zn}(\text{OH})_2$ or ZnO in an alkaline electrolyte. Thus, the process reduces dendritic growth. Stock et al.^[44] proposed an anion-exchange ionomer (AEI) coating on zinc electrodes to prevent oxidized zinc species and a confinement concept. A zinc oxide layer was formed between the AEI and the Zn electrode surface. The OH^-

could pass as expected. However, the Zn oxide layer impeded the oxidized zinc substance (Figure 4).

2.3.4 | Zn passivation

Zn passivation is the formation of an insulation metal surface. The dissolution of the zinc metal generates a solid zinc salt or hydroxide to cause a dense solid film on the electrode surface. The stability of the membrane determines the degree of passivation. Passivation of Zn anodes is formed by an insulating ZnO on the surface of the Zn anodes to prevent further electrochemical behavior.^[31] Zinc utilization rate is a commonly used measurement index of zinc electrodes. when the electrode is fully discharged, it is defined as the percentage of the theoretical capacity of zinc mass used. The stability of the Zn anode has a significant influence on the overall electrochemical performance of ZABs. In brief, there are three aspects: designing electrode interface modification, constructing new electrode structure, and exploring functional diaphragm to enhance the performance of Zn anode. The Zn electrode issue is limited to the commercial application of ZABs and requires further exploration by many researchers.

2.4 | Electrolytes

The role of electrolytes serves as a medium to conduct ions. Its components/proportions can directly determine

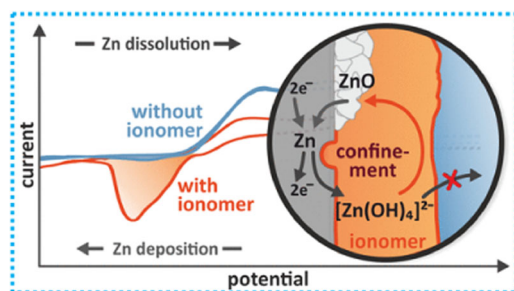
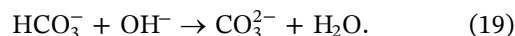


FIGURE 4 CV curves in 4 M KOH solution and the schematic illustration of confinement concept. Reproduced with permission: Copyright 2018, American Chemical Society.^[44]

the ionic conductivity and interfacial properties of the ZABs in operation. Moreover, it further affects the cell's capacity, cycling life, and charging/discharging efficiency. Choosing a proper electrolyte for ZABs is an urgent task to achieve better performance. In the following chapter, we will discuss the recent progress in electrolytes. The electrolytes of ZABs are generally divided into three types: aqueous electrolyte, solid electrolyte, and room-temperature ionic liquid (Table 1). The battery is a semiopen structure, and the air electrode part is in contact with the air. CO₂ in the outer atmosphere will pass via the air electrode and react with OH⁻ in the alkaline electrolyte or solid/quasi-solid electrolyte to generate carbonate or bicarbonate.^[45]



Carbonation can cause following problems: (1) The hydroxide ions (OH⁻) in the electrolyte or solid/quasi-solid electrolyte are consumed. The alkaline electrolyte is weakened and the performance of the battery is degraded. Moreover, it will cause the precipitation of ZnO in the Zn electrode, resulting in resistance increases and electrical conductivity decreases; (2) the formation of carbonate or bicarbonate will improve the viscosity of the electrolyte or block the solid/quasi-solid electrolyte ion channel, reducing the ionic conductivity; (3) the increase of the vapor pressure of the surface electrolyte accelerates the evaporation of the surface water; (4) after the carbonate or bicarbonate is saturated, it will crystallize on the air electrode, blocking the gas channels of the air electrode. Moreover, the change in water content is also an unavoidable problem for electrolytes or solid/quasi-solid electrolytes. When the air humidity is too large, the water vapor content will increase. The electrolyte is strongly alkaline and easily absorbs water, resulting in electrolyte concentration decrease, which will reduce ion conductivity. When the air humidity is too low, the water vapor content will drop. The moisture of the electrolyte or the solid/quasi-solid electrolyte will evaporate, causing the electrolyte concentration to increase, and the phenomenon of alkali climbing will occur, which will block the gas channels.

TABLE 1 Classification of electrolytes.

Different electrolytes	Advantages	Disadvantages
Aqueous electrolyte	High ion conductivity	Easily carbonated
Solid/quasi-solid electrolyte	Good leak-proof	Poor contact with air electrode
Room-temperature ionic liquids	Low volatility and insensitive CO ₂	Low ionic conductivity

TABLE 2 Blank electrolyte (KOH) with the addition of various additives.

Additive in electrolyte	Solutions	Effects
Organic additives ^[46–52]	Ethanol, DMSO, PEG SDBS, TAABs, TAAHs, CTAB, TEA, BPEI, EDTA, and so on	Suppress the generation of H ₂ , alleviate Zn corrosion, improve the hydrogen evolution potential, and discharge performance
Inorganic additives ^[53–57]	Na ₂ WO ₄ , Pb, ZnO, KF, In ₂ O ₃ , Bi ₂ O ₃ , SnO, K ₂ CO ₃ , silicate ion	Inhibit the formation of dendrites, avoid shape change

Abbreviations: BPEI, Polyethyleneimine; CTAB, Hexadecyl trimethyl ammonium Bromide; DMSO, Dimethyl-sulfoxide; EDTA, Ethylenediaminetetrace; PEG, Polyethylene glycol; SDBS, Sodium dodecyl benzene sulfonate; TAABs, tetra-alkyl ammonium bromides; TAAHs, Tetra-alkyl ammonium Hydroxides; TEA, Triethanolamine.

As briefly mentioned above, these problems will reduce the conductivity of electrolytes, and even the battery will not work in serious cases. ZABs must solve the problem of electrolyte volatilization and carbonate in the complex external environment. Recently, especially room-temperature ionic liquids (RTILs), ZABs have been proposed and evaluated. RTILs are alternative and effective solutions to solve the above issue. They can suppress the damage of Zn electrodes, slow down electrolyte drying out, achieve reversible oxygen reactions, and eliminate carbonation. However, their performance is constrained by their low ionic conductivity. The advantages and limitations of different kinds of electrolytes are summarized in Table 2. Thus, the chapter focuses on the progress and challenges of aqueous electrolytes, solid/quasi-solid electrolytes, and room-temperature ionic liquids.

2.4.1 | Aqueous electrolyte

Acidic and neutral electrolytes have been proposed for ZABs. Neutral and acidic electrolytes can efficiently minimize the formation of Zn dendrites. However, one critical problem is that the H⁺ concentration is quite low in neutral media, resulting in high overpotentials for OER. The violent reaction of Zn electrodes in the acidic solution causes severe metal anode corrosion. Therefore, neutral and acidic electrolytes are not suitable for use in practical applications. The alkaline solution is the most commonly used in ZABs owing to its high O₂ diffusion coefficient, excellent ionic conductivity, and low viscosity. Except for a few scattered reports, alkaline electrolytes (NaOH and KOH) are widely used. For comparison, zinc salts have higher solubility, a larger oxygen diffusion coefficient, and lower viscosity in KOH solution. Furthermore, the ionic conductivity of K⁺ (73.5 Ω⁻¹ cm² equiv⁻¹) is also better than Na⁺ (50.1 Ω⁻¹ cm² equiv⁻¹). Potassium carbonate (110.5/100 g water, 20°C) has higher solubilities than sodium carbonate (21.8/100 g water, 20°C).^[58] The potassium hydroxide and sodium

hydroxide react with CO₂ to generate carbonate or bicarbonate, which reduces ionic conductivity, and low solubility. Deposition on the air electrode causes the micropores to block the air electrode, hinder the entry of oxygen, and affect the ORR performance. For ZABs, KOH electrolytes are the most commonly used alkaline electrolytes. As revealed in Figure 5a, the ionic conductivity increases with increasing temperature. Experiments show that 6–7 M or 30% KOH has the highest ionic conductivity (about 620 mS cm⁻¹) at room temperature. Furthermore, Zn/Zn²⁺ exchange current density exhibits the highest value compared to other concentrations of KOH. Increased concentration of potassium hydroxide is accompanied by increased solubility of ZnO, suggesting that dendrites form rapidly during the charge and discharge process (Figure 5b). Dendrite formation and carbonate are the main causes of the performance decline of ZABs, which restrict the development of rechargeable ZABs in practical applications. Therefore, alleviating Zn dendrite formation and carbonation can effectively enhance the battery capacity, cycling stability, and charging/discharging efficiency. Recent studies have shown that appropriate additions could effectively improve electrochemical reversibility and reduce the occurrence of side reactions. As illustrated in Table 2, we summarize recent work showing the classification of various types of electrolytes in ZABs. In addition, various organic additives have also been studied in alkaline electrolytes due to the suppression of dendrite growth and H₂ evolution.

Lan et al.^[49] reported that the larger alkyl group and concentration of TAAHs could significantly control the growth of Zn dendrite, due to the physical adsorption of TAAHs. The alkyl groups can absorb the surface of Zn electrode to produce the blocking effect. Furthermore, TAAHs as additives into electrolytes did not influence ionic conductivity.

In another study,^[60] phosphoric acid, tartaric acid, succinic acid, and citric acid as additives to 8.5 M KOH solutions were compared with the without additives electrolyte. Research results reveal that the highest

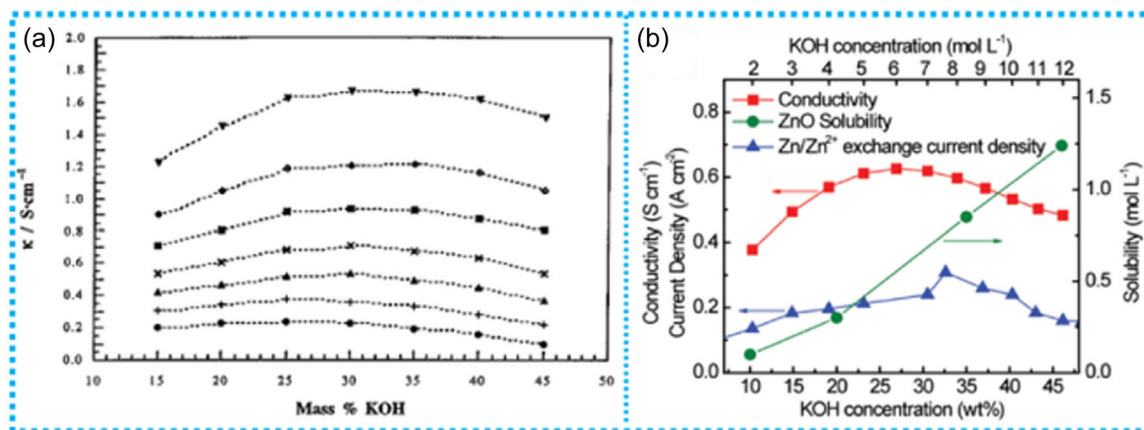


FIGURE 5 (a) The ion conductivity of the different concentrations of KOH in various temperatures. Reproduced with permission: Copyright 1997, American Chemical Society.^[59] (b) Conductivity, ZnO solubility, and Zn/Zn²⁺ exchange current density changing trends in the electrolytes. Reproduced with permission: Copyright 2017, Wiley-VCH.^[31]

number of polar functional groups was believed to be acting as a helpful suppression of dendrite formation due to purely electrostatic in nature.

Lee et al.^[61] reported that alkoxide and acetate ions could compete for a phenomenon for coordination to Zn²⁺ ions, forming modified zincate $\text{Zn}(\text{OH})_{4-n}(\text{OR})_n^{2-}$. Thus, the formation of zinc oxide (ZnO) could be effectively suppressed by adding alkoxide and acetate ions because $\text{Zn}(\text{OH})_{4-n}(\text{OR})_n^{2-}$ transforms into ZnO lower than that of $\text{Zn}(\text{OH})_4^{2-}$. The alcoholic additive can enhance the cyclability of batteries. The addition of 2% SDBS in an alkaline solution as a surfactant additive could effectively suppress surface passivation and greatly improve the capacity utilization of Zn anode due to the SDBS adsorption. The Zn surface formed a passive layer, which was a loose and porous structure. The porous surface layer greatly promoted the diffusive transportation of ions in the electrolyte to suppress the passivation of Zn electrodes.^[48]

2.4.2 | Solid/quasi-solid electrolyte

Under low current density, the aqueous ZABs have problems with uneven ion transport, leading to Zn dendrite formation. Meanwhile, under high current density, the battery will cause the instability of electrolyte flow to affect the battery performance. The aqueous electrolyte can raise leakage risk. Gel electrolyte (GPE) is a new kind of solid/quasi-solid phase material, which has good flexibility as well as mechanical properties. The appearance of GPE avoids these problems and promotes the further development of ZABs. The GPE electrochemical stability and mechanical strength are better than liquid electrolytes, and it is not easy to leak. In addition,

the solid electrolyte can provide relatively stable ion transport to make electrodeposition homogenization. Hence, it is considered one of the alternative materials for liquid electrolytes. Flexible ZAB configurations are generally divided into sandwich and cable types.

The sandwich ZABs are composed of an upper zinc anode, a middle solid electrolyte, and a lower air cathode. Another structure of flexible ZABs is cable type. The structure of the cable type is composed of a metal core, GPE wrapping metal core, and air cathode winding GPE.^[62] The GPE has some shortcomings in its practical application. During a long discharging/charging cycle, the liquid phase of GPE evaporates quickly, leading to inevitable encounter problems such as shrinkage, large ohmic polarization, and hardening. Therefore, simultaneously improving the water maintenance ability of GPE is an urgent problem. In the following section, we will review the recent advances in GPE, including polyvinyl alcohol (PVA), polyacrylic acid (PAA),^[63] and Polyacrylamide (PAM).

The structure of PVA is $-(\text{C}_2\text{H}_4\text{O})_n-$, which has been widely employed as a GPE because of its easy-to-prepare, nontoxic, good chemical and electrochemical stabilities. The PVA possesses a high content of hydroxy to provide a critical chance for substitution/modification.^[64] The hydroxy can have a mutual affinity to form a large hydrogen bond in the molecular internal, leading to the weak physical interaction of GPE inside and strong water absorption ability. However, the compactness of the GPE affects water retention performance, thus resulting in GPE drying up. To deal with the problems, various strategies have been investigated, such as the functional modification of electrolytes and the addition of additives (water-retaining agents or others). Zhou et al.^[45] illustrated a prefixation of CO₂ on PVA (named PVA-TMG) through the ionization method and the structure of the quasi-solid-state ZAB (Figure 6a). As shown in

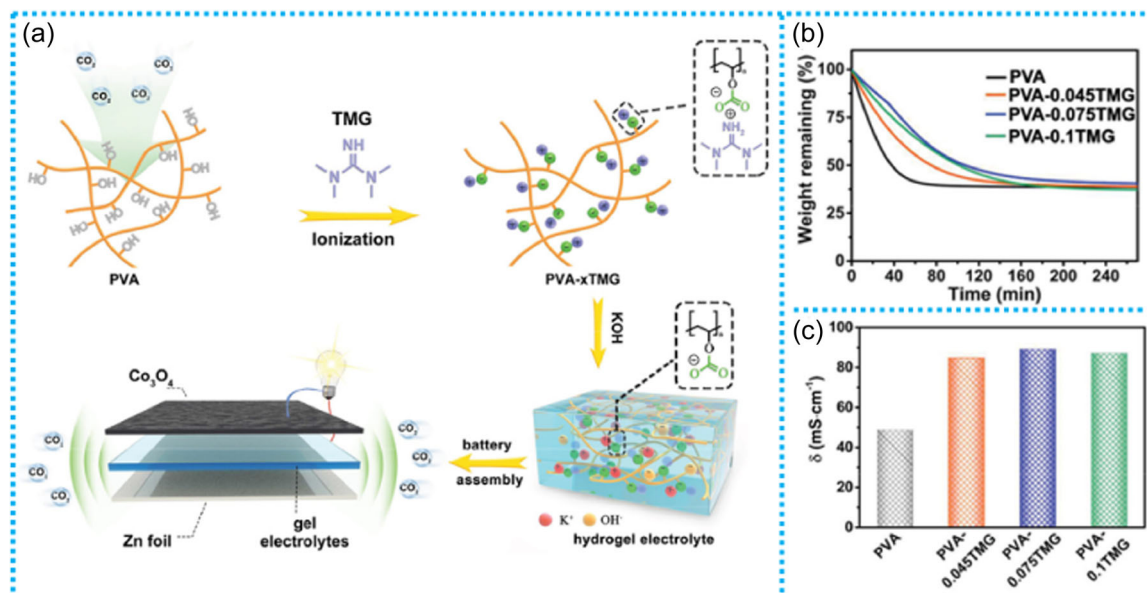


FIGURE 6 (a) Schematic showing the preparation of the GPE and its application. (b) Water maintenance ability. (c) The electric conductivity of the corresponding GPEs. Reproduced with permission: Copyright 2021, Wiley-VCH.^[45]

Figure 6b, to determine the water retention capability of the electrolyte, the loss water rate of PVA-xTMG GPE with 3 M KOH was analyzed by thermogravimetric analysis (TGA). The PVA-0.075XTMG presented the best water retention capability than the pristine PVA and showed a maximum ionic conductivity due to the polar side $-\text{OCO}_2^-$ group existing (Figure 6c). Designing the PVA-based GPE by the functional modification tetraethylammonium hydroxide (TEAOH-PVA) that could efficiently stabilize water molecules and showed an excellent ionic conductivity than the PVA-KOH GPE. The TEAOH-PVA detected no carbonate hydrate precipitates peak by X-ray diffraction analysis (XPS) in the open system for 72 h, illustrating a good tolerance for CO₂. The fresh TEAOH-PVA-GPE-based ZABs had a cycle stability of more than 30 h. After storage for 15 days, the TEAOH-PVA-GPE-based ZABs still maintained their original shape for cycle life, whereas the PVA-GPE-based ZABs had dropped severely.^[65]

Wu et al.^[66] meaningfully prepared hybrid PVA and PAA via the solution casting method. This approach prepared a highly uniform hydrophilic membrane. The ionic conductivity of the alkaline PVA/PAA GPEs was approximately 0.142–0.301 S cm⁻¹ at room temperature. The PVA/PAA GPEs (ratio = 10:7.5) display excellent ionic conductivity (0.301 S cm⁻¹) at room temperature. The PVA/PAA GPEs as ZABs electrolytes presented a retention rate of high capacity and power density. Despite great progress in GPEs, high-performance rechargeable flexible ZABs are still necessary for further improvement in ionic conductivity, water-retaining capacity, and mechanical strength.

The structure of PMA is $-(\text{C}_3\text{H}_5\text{NO})_n-$, which has receive extensive attention due to high stretch-ability, ion transport capability as well as low crystallinity. Considering this characteristic of PAM, numerous works has been studied on flexible ZABs using PAM as GPE electrolytes. For instance, Miao et al.^[67] reported the PAM GPE with 3 g Acrylamide (AM) and 20 wt% KOH. Figure 7a showed the photograph of the PAM GPE crimping, demonstrating good mechanical properties. And the water retention rate of the PAM GPE was the best due to its porous structure (Figure 7b). The PAM GPE possessed much higher conductivity (215.6 mS cm⁻²) than the PVA GPE in Figure 7c. The PAM-based AGE displayed an outstanding water retention rate of 86.6% after 144 h (Figure 7d). As schematically illustrated in Figure 7e,f, the PAM GPE as ZAB electrolyte exhibited a maximum power density and the smallest potential gaps. Moreover, the PAM GPE as ZAB electrolyte could remain normal work under bending, twisting, pressing, and cutting. By comparison, traditional unmodified GPEs displayed inferior properties at wide-window temperatures. Zhang et al.^[68] reported dual-surfactant-optimized GPE (PAM-F/G). The PAM was modified by dual surfactants (GO and pluronic F127). The PAM-F/G in immersing 6 M KOH solution formed the PAM-F/G GPE. The flexible ZAB using PAM-F/G electrolyte exhibited excellent mechanical properties, ionic conductivity (276 mS cm⁻¹ at 20°C), as well as an outstanding power density of 155 mW cm⁻² at 20°C. Moreover, the PAM-F/G GPE could be applied in a cold environment. In addition to the PAM-based GPE applied

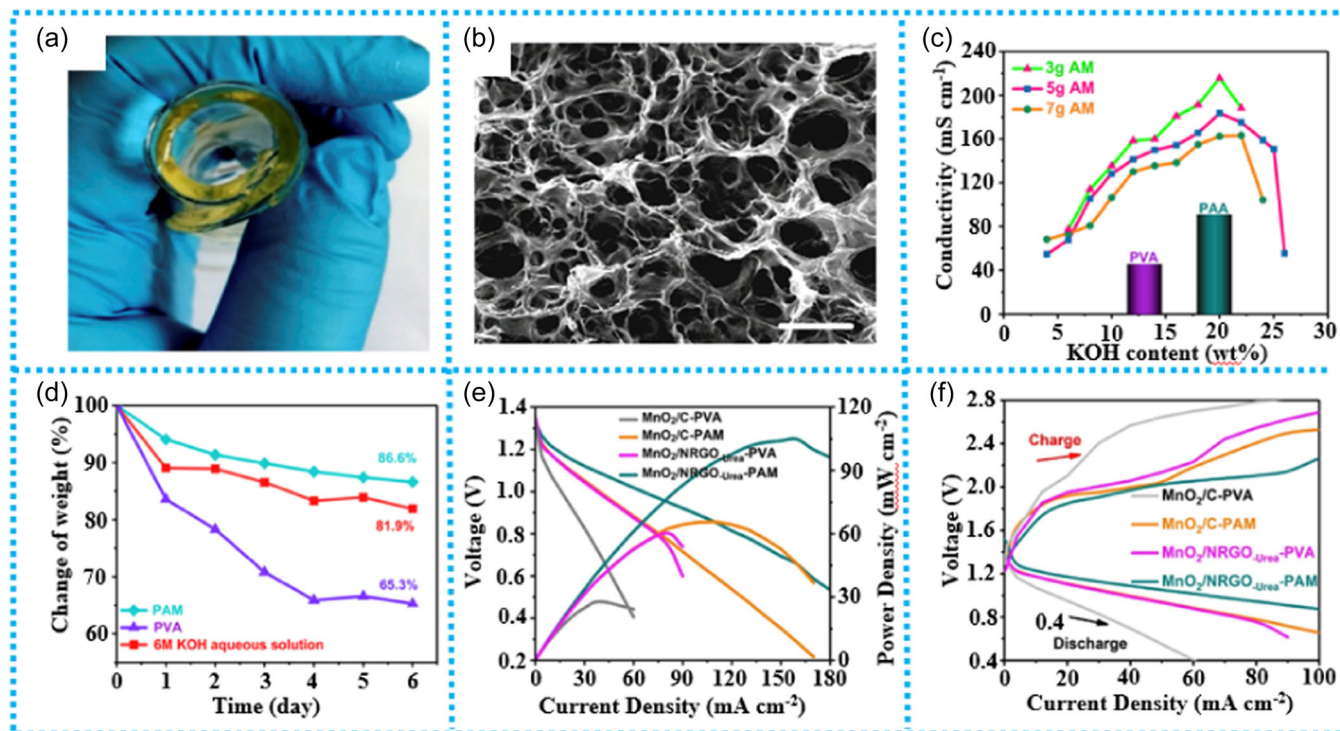


FIGURE 7 (a) A photograph of bending PAM GPE. (b) Morphology characterization of PAM GPE. (c) Various AM contents in KOH solution of PAM GPE. (d) the water retention rate of PAM, 6 M KOH solution, and PVA in an open system. (e) Power density of different materials in PAM or PVA electrolyte. (f) Charge/discharge curves of different materials in PAM or PVA electrolyte. Reproduced with permission: Copyright 2020, Elsevier Ltd.^[67]

in ZABs, it is also widely developed in solid-state flexible supercapacitors^[69–72] and zinc-ion batteries.^[73,74] Through acrylamide (AM) and acrylic acid (AA) double cross-linked (PAAK-M), the traditional GPE has been improved in mechanical properties, ion conductivity, and water retention capacity. The PAAK-M-based ZABs deliver an excellent power density and a long discharge/charge cycle life at a wide temperature range.^[75]

The structure of PAA is $-(CH_2-CHCOOH)_n-$, which possesses a large functional carboxyl group to obtain good water retention. And, the unmodified GPEs (PVA, PAA, and PAM) with 6 M KOH were studied.^[76] The PAA GPEs with 6 M KOH solution had the highest conductivity (204 mS cm^{-1}) than PVA and PMA GPEs. However, the PAA-based GPEs displayed comparatively bad mechanical stiffness that made GPEs prone to collapse and a remarkable increase in resistance value. Song et al.^[77] prepared a PAA- Al_2O_3 GPE by the solution polymerization method. When the PAA was added 30 wt % Al_2O_3 annexing agent, the mechanical strength of PAA- Al_2O_3 GPE also increased to the maximum, but the water retention and ionic conductivity dropped, suggesting the importance of the suitable Al_2O_3 content. The PAA- Al_2O_3 (the content of 20 wt% Al_2O_3) GPE-based ZABs exhibited a long-term discharge/charge life (305 h). Guo

et al.^[78] reported a supramolecular PAA GPE ($KCl-Fe^{3+}/PAA$), which was prepared through the polymerization process. The ionic and hydrogen bond of $KCl-Fe^{3+}/PAA$ GPE endowed a good self-healing ability. Moreover, the $KCl-Fe^{3+}/PAA$ GPE displayed an outstanding ion conductivity (90 mS cm^{-1}), and Li et al.^[79] prepared a mixing electrolyte (cellulose nanofibril [CNF] and PAA). The GPE not only possessed the mechanical strength of CNF but also remained the ionic conductivity of PAA. Although the flexible battery has made great progress, further improvements in ionic conductivity, water retention capacity, and mechanical strength are necessary for the practical application of flexible devices.

2.4.3 | Room temperature ionic liquid (RTILs)

Ionic liquids (ILs) are liquid ionic salt substances at room temperature.^[80] Compared to the aqueous electrolyte, the ILs solved the evaporation of electrolytes and the reaction between electrolytes and CO_2 in open systems, due to extremely low vapor pressure and no alkaline solution in the electrolyte. Therefore, ILs became a research hotspot in the field of electrolytes. The ILs are composed of the anion

(imidazoles, pyrroles, quaternary ammonium salts, quaternary phosphorus salts, thiazoles, and so on) and cation (Cl^- , CH_3SO_3^- , BF_4^- , PF_6^- , Al_2Cl_7^- , and so forth). Owing to the diversity of organic cation and inorganic anion combinations, the ILs have several ways to arrange. Importantly, the cations or anions of ionic liquids can be partially modified, adjusting their physical/chemical properties. The RTILs can be obtained by increasing the volume and structural asymmetry of cations or anions and weakening the interaction between anions and anions, which leads to accumulating crystals. The RTILs have many advantages (low volatility, nonflammability, high thermal stability, and environmentally friendly).^[81] Despite RTILs having so many advantages, their electrochemical properties are still significantly inferior to the alkaline electrolyte due to their low conductivity and high viscosity. Therefore, the RTILs introduce special functional groups (hydroxyl, carboxyl, and ether) or additives (water and ZnCl_2) to further improve the RTILs performance. For instance, Xu et al.^[82] designed an RTIL (1-butyl-1-methyl-pyrrolidinium bis (trifluoromethane-sulfonyl)imide (BMP-TFSI)) with water as an additive agent. As a result, the contained water of additives could affect Zn/Zn(II) redox behavior. The type of water was analyzed by FTIR analysis and density functional theory (DFT). When the water content was ~ 2.0 wt%, water molecules combined with $[\text{TFSI}]^-$ anions to entirely form bound water. Among RTILs, 2.0 wt% water addition reduced the overpotential of electrochemical reactions and enhanced ion conductive to improve Zn/Zn(II) redox reversibility. Therefore, the addition of water could improve conductivity and high viscosity. In addition, a change of nature selects appropriate anions or cations, which are feasible to adjust zinc electrodeposition. Simons et al.^[83] studied $[\text{X}]\text{DCA}$ (X: 1-ethyl-3-methylimidazolium (C_2mim) or N-butyl-N-methylpyrrolidinium (C_4mpyr) for the electrochemical behavior of Zn. For comparison, the $[\text{C}_2\text{mim}]\text{DCA}$ containing 3 wt% H_2O and 9 mol% Zn (DCA)₂ greatly reduced Zn deposition overpotentials and good current density with cycling performance. At present, the ion conductive and electrochemical property of RTILs is considerably inferior to aqueous KOH electrolyte. Moreover, the high cost of ILs also impedes their practical application in ZABs.

3 | AIR ELECTRODES (GAS-DIFFUSION LAYER (GDL) AND CATALYSTS)

3.1 | GDL

As one of the most significant parts of an air electrode, the gas-liquid-solid three-phase interface mainly happens in the place of ORR and OER. The GDL (such as

carbon cloth and carbon paper) is made up of hydrophilic (active carbon) and hydrophobic parts (polytetrafluoroethylene [PTFE], Poly(vinylidene fluoride) [PVDF], and fluorinated ethylene propylene [FEP]). Among them, the addition of PTFE can regulate the hydrophobicity of the GDL.^[84] Therefore, the content of PTFE is reasonably controlled to resist leakage and attain optimal air diffusion performance under extreme conditions.^[5] The GDL can allow air to enter while limiting liquid electrolyte spills. And, the O_2 gas through the GDL is significantly faster than that of through the electrolyte due to most solutions' low oxygen solubility at room temperature (about 10^{-3} – 10^{-4} mol l⁻¹). The GDL has provided the functions of physical support, acting as an oxygen diffusion channel and preventing electrolyte leakage. The ideal GDL should have fast air diffusion to meet the needs of the catalytic layer. To get the best out of ZABs, the GDL should possess porous, excellent conductivity, good stability, and corrosion/oxidation resistance to provide enough reaction space.^[85] However, the corrosion of GDL causes the gradual decay of the cycle life of ZABs due to the high oxidation potentials and alkaline electrolytes. Among GDL, the active carbon is highly susceptible to resulting in the collapse of the GDL structure and the leakage of alkaline solution. For long-term cycle life, the GDLs can use high graphitization carbon materials or metallic substrates (stainless-steel mesh and nickel/copper foam to prevent the corrosion of the hydrophilic part.

3.2 | Air electrode catalysts

Currently, the air electrode is divided into GDL, current collector, and catalyst layers. To achieve high efficiency of RZABs, the air electrode must possess excellent catalytic activity and stability. In general, the air electrode is a sandwich structure. Specifically, the catalyst layer is covered on a current collector and in contact with the electrolyte. The current collector is placed between the catalyst layer and GDL. The ORR and OER are the most important reactions of the ZABs. In the bifunctional catalyst, the potential difference (ΔE) between the potential of 10 mA cm^{-2} OER and the half-wave potential of ORR is usually used as a parameter to measure the bifunctional performance of the catalyst.^[86] Smaller ΔE means lower efficiency loss and better bifunctional performance. Precious metals or their oxides (Pt, IrO_2 , RuO_2 , etc.) exhibit an outstanding single catalytic performance and accelerate ORR or OER kinetic processes, but they are scarce, high cost, and lack dual-function properties.^[87] These properties severely hampered the large-scale commercial application of

reversible ZABs. In recent years, researchers have made great efforts to develop nonprecious alternatives. Moreover, it opens up new opportunities for designing non-noble metal bifunctional catalysts, which possess low reaction energy barriers, overpotential, and high stability. In the following sections, we summarize the application of bifunctional electrocatalysts as air electrodes in rechargeable ZAB, such as carbon-based nonmetallic catalysts, transition metal-based catalysts, and so forth. Summary of recent advancements in CB-MFM toward electrocatalytic property is listed in Table 3. Based on the above considerations, accelerating the ORR/OER dynamic process and mitigating the corrosion of air electrode catalysts are the fundamental ways to improve the performance of reversible zinc-air batteries.

3.2.1 | Air electrode CB-MFM catalysts

Nonmetallic carbon materials have attracted much attention due to their large specific surface area, good chemical stability, and high conductivity, especially

carbon nanotubes, carbon fibers, carbon nanosheets, and graphene, which show great potential in the catalytic process. However, most of the original carbon electrocatalysts (carbon black, carbon nanotubes, and graphene) are generally inactive for ORR and OER because of the lack of active sites when adsorbing/desorbing O₂ and other intermediates.^[7,8,106,107] Therefore, it has poor intrinsic activity. Moreover, the structure of carbon material is easy to be corroded under high potential, which reduces the stability of the catalyst. To obtain high catalytic activity, the introduction of heteroatoms (such as N, P, S, O, and B) or defects in the metal-free carbon catalyst will change the charge density of the local area of the carbon atom to create more active sites, and then improve the ORR and OER catalytic activity.^[25,92,100,108] As shown in Figure 8, 5 different heteroatoms replace the edge or center carbon atoms of graphene, resulting in 15 different doping configurations.^[109]

Boron is located in the period 2 and group 3 of the periodic table. The electronegativity of B (2.04) is lower than that of the carbon atom, and the atomic radius of B (82 ppm) is similar to that of the carbon atom (77 ppm), which

TABLE 3 Summary of recent advancement in CB-MFM.

Catalysts	E _{1/2} vs. RHE (V)	Overpotential (mV)	Peak power density (mW cm ⁻²)	Cycling stability (x = h, y = mA cm ⁻²)
N-GRW ^[88]	0.84	360	65.0	30 x at 20 y
GH-BGQD ^[89]	0.88	380	112.0	/
PCN-CFP ^[90]	0.67	400	/	/
CF-K-A ^[91]	0.83	/	61.5	/
NPS-G ^[92]	0.85	/	151.0	/
NGM ^[25]	0.77	440	/	/
N-SMCT ^[93]	0.87	351	126.0	85 x at 10 y
CNRs-C ^[94]	0.90	420	259.1	80 x at 5 y
NPCNF-O ^[95]	0.85	326	125.1	200 x at 5 y
N-CNTs ^[96]	0.80	470	195.2	350 x at 10 y
NPCSS ^[97]	0.83	320	79.0	56 x at 2 y
SHG ^[98]	0.87	410	/	/
BNF-LCFs ^[99]	0.84	342	99.4	/
NPMC-1000 ^[100]	0.85	/	55.0	100 x at 2 y
NPC-950 ^[101]	0.88	371	184.5	85 x at 20 y
NSP-Gra ^[102]	0.82	430	225.0	/
N-GDY-900 ^[103]	0.83	566	115.0	300 x at 5 y
BP-CN-c ^[104]	0.84	350	168.3	300 x at 10 y
VGNO ^[105]	0.83	490	221.9	300 x at 10 yPF

Abbreviations: CB-MFM, carbon-based metal-free material; RHE, reversible hydrogen electrode.

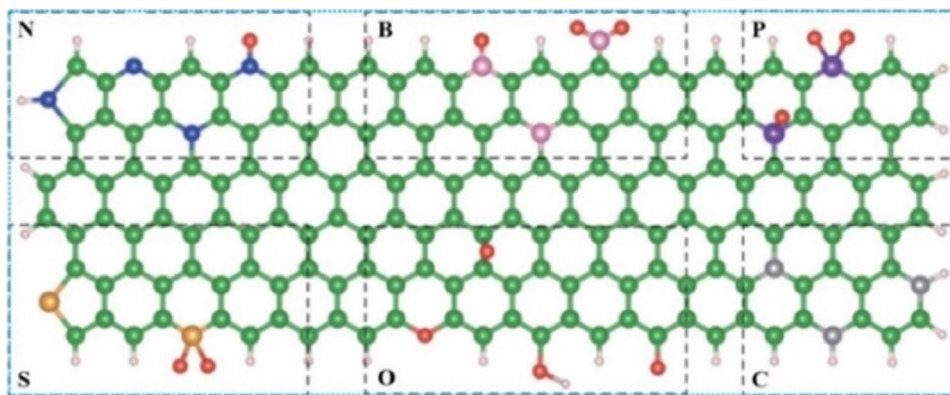


FIGURE 8 Schematic diagram of heteroatom doping configuration green/gray, pink, blue, red, gold, purple, and white represent C, B, N, O, S, P, and H atoms, respectively. Reproduced with permission: Copyright 2016, Springer Nature.^[109]

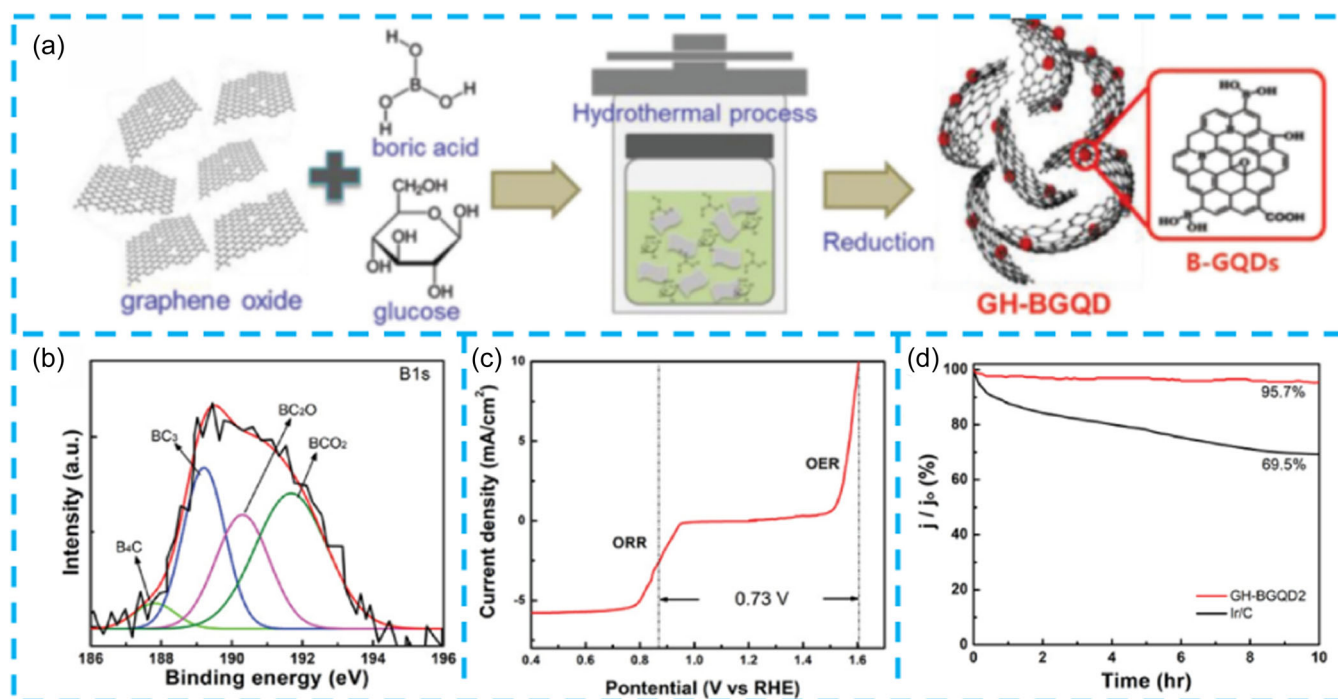


FIGURE 9 (a) One-pot synthesis diagram of GH-BGQD. (b) Fitting of B1s peak of GH-BGQD. (c) The polarization curve of GH-BGQD2 showed its bifunctional activity to ORR and OER. (d) I-t curve of GH-BGQD2 and Ir/C. Reproduced with permission: Copyright 2019, Wiley-VCH.^[89]

increases the hole carriers and promotes the effective adsorption of negatively charged oxygen atoms. Su et al.^[110] designed a boron doping mesoporous carbon material (B-C-2) through a self-assembly process. Benefiting from the high specific surface area, ordered mesoporous structure, and B-C active sites, the B-C-2 exhibited a higher ORR activity. Furthermore, Tam et al.^[89] used a simple hydrothermal method to anchor boron-doped graphene quantum dots on graphene aerogels (GH-BGQD) in Figure 9a. As described in Figure 9b, GH-BGQD2 had the highest BC_3 structure and high BC_2O and BCO_2 bonding.

The DFT results showed that the BC_3 structure in the composite had a high oxygen adsorption energy and an excellent electron-transport property, leading to its excellent ORR performance. However, the negative charge of the oxygen atom in BCO_2 interacted with the H atom in OH^- , and the positive charge of the boron atom interacted with the O atom in the H_2O molecule, which promoted the adsorption of OH^- and H_2O , accelerating the OER and HER processes. GH-BGQD composite material showed obvious three-function electrocatalysis performance and had good stability in an alkaline medium (Figure 9c,d).

In addition to boron atom modification, other heteroatoms (P, S, N, etc.) can also adjust the electrochemical performance of carbon materials after modifying carbon materials. The different electronegativity compared with adjacent carbon atoms. The carbon-based material can adjust the local electronic environment and increase the density of active sites, which is conducive to the adsorption/desorption of oxygen intermediates, thus improving the catalytic performance. Phosphorus is located in the period 3 and main group 5 of the periodic table. The P atom possesses a large atom radius (110 pm) and low electronegativity (2.10) compared to the carbon atom (77 pm, 2.55). P atom can elongate C-P and adjacent C-C bonds to form pyramidal-like and lattice distortion-induced defects.^[111] Moreover, the P atom can act as an electron donor due to the outer electrons weak attraction. According to the above description, the doping of the P atom in the carbon matrix can cause electronic redistribution. The adsorption strength of oxygen molecules and intermediate substances in the active sites is changed. Zhang et al.^[112] simply annealed the graphite oxide and triphenylphosphine to obtain P-doping carbon material (PG). The as-synthesized PG showed a higher ORR performance than the G material. To explore the catalytic mechanism of P doping carbon material, theoretical calculation was conducted. Zhang et al.^[113] investigated the mechanisms of ORR on P-doped graphene using the first-principles study. The research exhibited that the dopant region

could conduct all of the ORR. Moreover, the reaction proceeds to undergo the $2e^-$ process to achieve OOH intermediate at the beginning and is followed through the $4e^-$ process to fracture the O-O bond. The P dopant could regulate the electronic and geometric structure of the carbon matrix, which was deemed to be the efficient pathway to improve ORR activity.

To investigate further, Yang et al.^[114] explored the P dopant sites in the carbon skeleton to verify the optimal structure. As illustrated in Figure 10, pristine and four configurations of P-doped graphene were rationally designed and constructed to survey the effect of P-dopant sites on the ORR catalytic activity. The theoretical calculation demonstrated that the P dopant sites and the introduction of O in the C-P bond could effectively adjust the stability and free energy for ORR. Moreover, the charge of the carbon atom was redistribution due to the introduction of the P atom. Interestingly, the C atoms were also regarded as an efficient active site. In conclusion, the P-doped can change the local chemical environment and lattice distortion-induced defects, which affect the ORR performance. However, many complicated factors make the real mechanism obfuscation for ORR.

According to the above statement, breaking the electronic distribution of the graphene skeleton is crucial to enhance ORR activity. Sulfur is located in the period 3 and main group 6 of the periodic table. The electronegativity of the Sulfur atom (2.58) is extremely close to

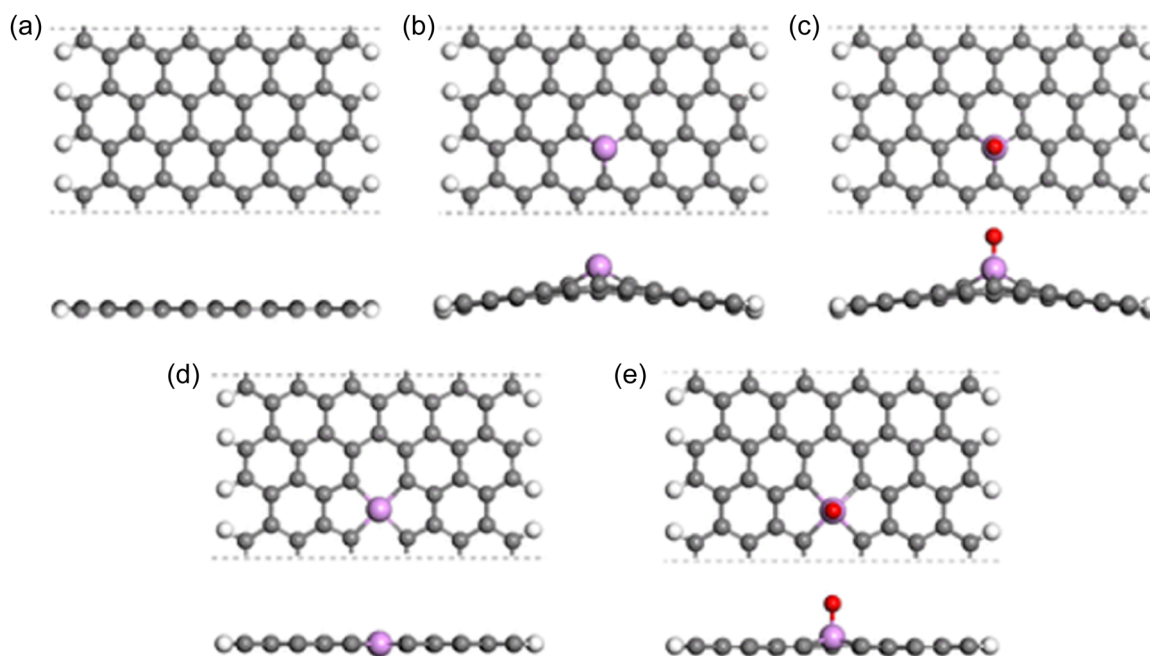


FIGURE 10 Top and side views model of graphene skeleton (a), PC3G (b), OPC3G (c), PC4G (d), and OPC4G (e). Reproduced with permission: Copyright 2017, American Chemical Society.^[114]

the carbon atom (2.55). When the dopant atom has similar electronegativity, the produced effect has attracted many researchers to investigate its mechanism. Yang et al.^[115] directly annealed the graphite oxide and benzyl disulfide to prepare S-doped graphene (S-graphene-X). The spin density was identified as the main factor in determining the active center.^[116] The S-doped can cause a small change in atomic charge distribution in the carbon skeleton. Therefore, the spin density is deemed to regulate the main factor of ORR activity. To further explore catalytic mechanisms of S modification graphene, Zhang et al.^[117] predicted the S-doped graphene clusters through DFT. The S/S oxide and S cluster ring model was constructed to verify the active center. The result demonstrated that catalytic active units could be divided into two parts (S-doped zigzag edge and the adjacent C atom of S oxide), which had a positive charge and spin density. Among the S-doped graphene clusters, the S part with high charge density could occur in two-electron transfer processes while the C part with high positive spin appeared in a four-electron transfer pathway. And, the S-doped graphene was predicted a comparable Pt for ORR activity. In addition, other S-doped configurations also needed to be discussed, such as graphitic sulfur-doped graphene. Lu et al.^[118] investigated the detailed ORR process on S modification monovacancy graphene (SGv) through the first-principles method. The mechanism was proposed pathways on SGv (the dissociation and hydrogenation of OOH*). The energy barriers of the two proposed processes were 0.75 and 0.62 eV. The OOH* dissociation could be precluded due to the endothermic from O to OH. Thus, SGv could improve an efficient electrocatalytic activity for ORR.

Heteroatom N-doped carbon materials have been investigated in depth owing to their remarkable activity and inexpensive. The introduction of N atoms in the carbon skeleton breaks an equilibrium state and generates the adjacent C atoms charge delocalization. Adjusting electron density provides a wide space for improving the performance of CB-MFM. Thus, the local position is treated as an efficient active site, thereby improving the catalytic activity. Therefore, the insertion of nitrogen atoms into carbon materials is one of the most effective ways to obtain efficient ORR catalysts. Nitrogen-doped carbon materials are wonderful low-cost catalysts for ORR. It is worth mentioning that biomass-derived carbon materials as metal-free ORR electrocatalysts have also attracted great attention. For example, nitrogen-doped carbon catalysts with unique hierarchically porous structures (N-WPAC) were synthesized using watermelon peel as a precursor through KOH activation and subsequent nitrogen doping. The N-WPAC displayed a

superior ORR ability and stability ascribing to its hierarchically porous carbon structure with abundant defects ($S_{\text{BET}} \approx 782.69 \text{ m}^2 \text{ g}^{-1}$ and pore volume $\approx 0.44 \text{ cm}^3 \text{ g}^{-1}$), which was beneficial to expose sufficient active sites and accelerate the reaction-transfer.^[119] Similarly, Zhao et al.^[120] used soybean shell as precursor material and mixed KHCO_3 to attain N-doped porous carbon (NPC) with a high S_{BET} of $1036.2 \text{ m}^2 \text{ g}^{-1}$ by a pyrolysis method in the N_2 atmosphere. Owing to N in-situ doping, the NPC showed favorable ORR capability, and NPC-based ZABs had a high open-circuit voltage (1.27 V). So that, some catalytic mechanisms of n-doped carbon electrocatalysts have been proposed. One mechanism suggests that the insertion of the N dopant induces changes in the charge and spin distribution of adjacent C atoms because of the higher electronegativity of N over C, which benefits oxygen adsorption and dissociation. In 2009, Gong et al.^[11] first reported vertically aligned nitrogen-doped carbon nanotubes (VA-NCNTs) electrocatalysts. The VA-NCNTs exhibited comparable activity and superior durability in comparison to Pt/C. Several possible reasons for electrocatalytic performance are superior: (1) the incorporation of nitrogen reveals a comparatively high positive charge density on neighboring carbon atoms which induces charge delocalization to change the chemisorption mode of O_2 reactant from the Pauling model to the Yeager model and thus effectively reduces energy barrier of O–O bonds cleavage. (2) the large external SSA promotes the rapid diffusion of electrolytes, oxygen, and intermediates. Guo et al.^[121] adjusted the composition structure and pore size of sp³ and sp² hybrid carbon, so that the 3D N-doped nano carbon surface had a high sp³/sp² carbon ratio, showing excellent ORR electrocatalytic performance. Density functional theory calculation showed that the improvement of ORR performance was attributed to the existence of N atoms at the sp³/sp² carbon interface, which changed the distribution of charge density and can reduce the theoretical overpotential of ORR.

Further studies show that pyridine nitrogen, pyrrole nitrogen, nitrogen oxide, and graphite nitrogen can be formed on carbon matrix by different bonding configurations of nitrogen dopants. The type of N doping has a great influence on the properties of carbon materials. Thereafter, a variety of nitrogen types with carbon atoms have been reported to display high-efficiency ORR electrocatalysts. As a typical example, Zhang et al.^[122] reported a pyridinic-N dominated and 3D porous nanocarbon material (ND-GLC) with outstanding ORR activity and stability in both rotating disk electrode measurements and ZABs. Importantly, the synergistic effect of defects structure and pyridinic-N dopants determined the whole catalytic activity.

Moreover, this method could be demonstrated to be universal for other carbon-based nanomaterials (i.e., graphite nanoplates, carbon nanotubes/nanospheres, and graphene nanosheets). In this context, Wang et al.^[123] used alkali to activate carbon aerogels, and then used the N modification strategy to prepare nitrogen-doped carbon nanoparticles. The results showed that the high catalytic activity of NKCNP-900 came from the high content of pyridine N and graphite N. At the same time, its high specific surface area, rich edge defects, and mesoporous structure could expose more active sites and accelerate the wetting of carbon materials during the catalytic reaction. Many literatures reported that pyridine N as the electrocatalyst of ORR may be more active than pyrrole N and graphite N in carbon materials. Therefore, to explore the efficient catalyst of ZABs, it is very important to controllably dope specific styles of N. Zhou et al.^[124] successfully synthesized nitrogen-doped hollow mesoporous carbon spheres (NHCSs) through a simple hydrothermal method. The content of graphite N and pyridine N in NHCSs-X (annealed at 800°C, 900°C, and 1000°C respectively) increased as the temperature rose. NHCS-1000 showed good ORR activity and long-term durability because pyridine and graphite N are dominant species.

The single N-doped carbon material is also of great significance for the mechanism study. However, it is very challenging to obtain N-doped carbon catalysts

containing only one type of N. A few studies have confirmed that Lv et al.^[125] prepared a pyridine N configuration (PyN GDY) using pentaacetylpyridine as a precursor to accurately control the configuration of N atoms in the carbon matrix. As shown in Figure 11a, the prepared PyN GDY catalyst contained rich graphyne and pyridine nitrogen structures. In the peak fitting of N, only one 399.9 eV pyridine N peak appeared (Figure 11b). In Figure 11c,d, PyN-GDY showed excellent ORR characteristics and fast reaction kinetics, which were similar to Pt/C. The good activity of PyN GDY came from the pyridine N structure. According to the density functional theory (DFT) calculation, the catalytic activity of pyridine N was superior to that provided by graphitized N. Although nitrogen-doped carbon materials showed excellent ORR activity, they had poor OER activity. These studies revealed that it was imperative to precisely construct the specific nitrogen-doped carbon material.

Compared with single atom modification, multiple (binary or ternary) modifications can produce rich structural diversity and more effectively adjust the local electron density, which is conducted to further improve electrocatalytic activities. Fei et al.^[126] prepared graphene quantum/graphene (GQD/G) and then obtained BN-codoped GQD/G using boric acid as the B source and Ar/NH₃ (300/30 sccm) as a nitrogen source. The BN-codoped GQD/G material possessed an abundant edged and doping unit. The optimized material displayed

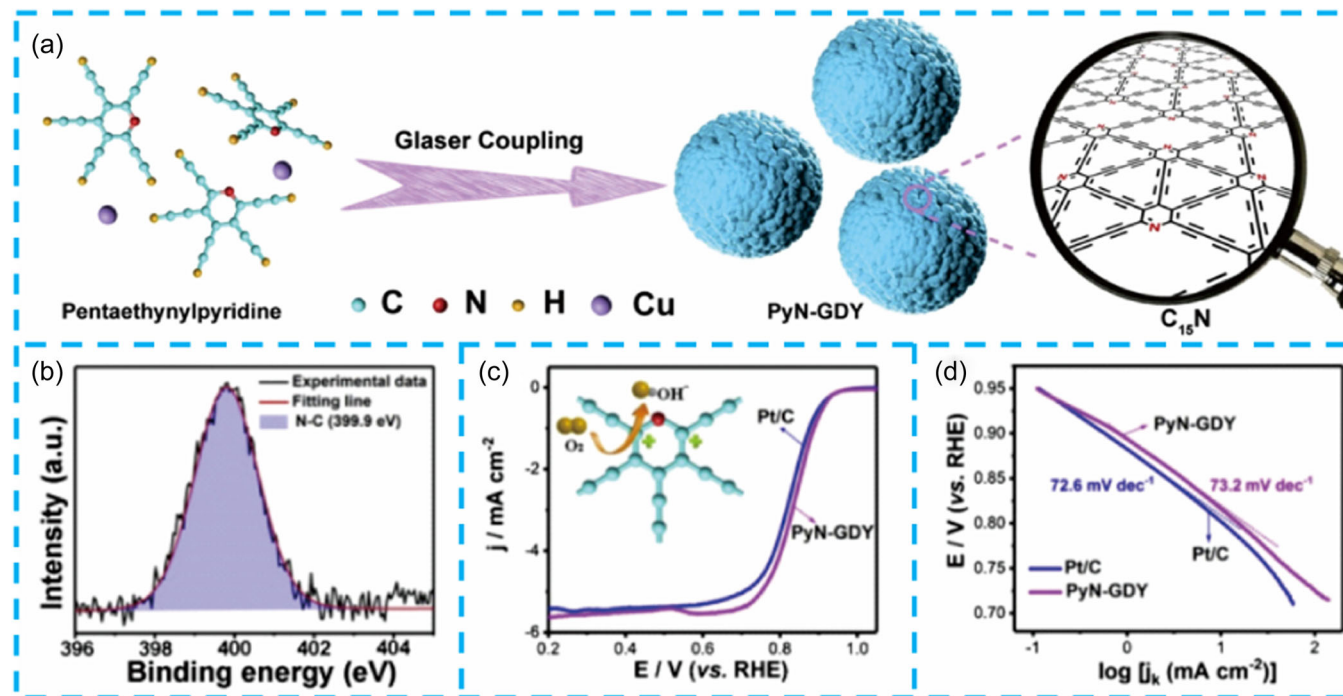


FIGURE 11 (a) Synthetic diagram of PyN-GDY. (b) Peak fitting of N1s of PyN-GDY. (c) Polarization curves of PyN-GDY and Pt/C. (d) Tafel curves of PyN GDY and Pt/C. Reproduced with permission: Copyright 2020, Elsevier Ltd.^[125]

excellent ORR performance. Zhao et al.^[127] reported a B, N doped ultrathin carbon nanosheet using NaCl-assisted anneal. The introduction of the B atom could improve local electron structure and O₂ adsorption. Thus, the BN/C showed a preferable ORR activity. Zhang et al.^[128] disclosed a new method to control the doping position of B in the graphene framework. The C atom was polarized by the adjacent N atom and then could donate extra electrons to the B atom. This process activated the B atom and induced a synergistic coupling to facilitate the ORR reaction due to the charge transfer process. To further probe the various N-B configurations, Fan et al.^[9] directionally prepared pyridine N-B (BN-C-1) to modify two carbon structures (crystalline graphene nanoribbons and amorphous porous structures) through the “double catalysis” (Fe salt, H₃BO₃) strategy. The B-N bond type was easily constructed owing to the large distinction in electronegativity of the two atoms. Subsequently, the four B-N configurations were designed to study the catalytic mechanism (Figure 12a). From Figure 12b,c, the B@PyN exhibited a low overpotential and was located at the top

of the volcano, demonstrating that the sample material possessed excellent ORR activity. In Figure 12d,e, the B@PyN occupied more pz orbits electron than other B-N configurations. As displayed in Figure 12f, the adjacent C atom of the B atom was the electron concentration site, which was the active center. Moreover, the section had proper OH/OOH adsorption. Among all nitrogen types, pyridine N-B of BN-C-1 accounts for 80%. Benefiting from these structures, its ORR catalytic performance was close to commercial Pt/C and superior to most previous carbon-based catalysts.

Ma et al.^[90] reported a flexible nonmetallic material. The P-modified g-C₃N₄ was grown on carbon cloth (PCN-CFP) via a hydrothermal process. The introduction of the P atom can adjust the electronic structure, improving the conductivity. The PCN-CFP showed high ORR and OER performance and stability due to the introduction of P and N. Zhang et al.^[100] discussed N and P co-doped mesoporous carbon foam (NPMC). The N and P atoms in NPMC material might exist in various forms (single N/B and co-N, P dopant). According to the

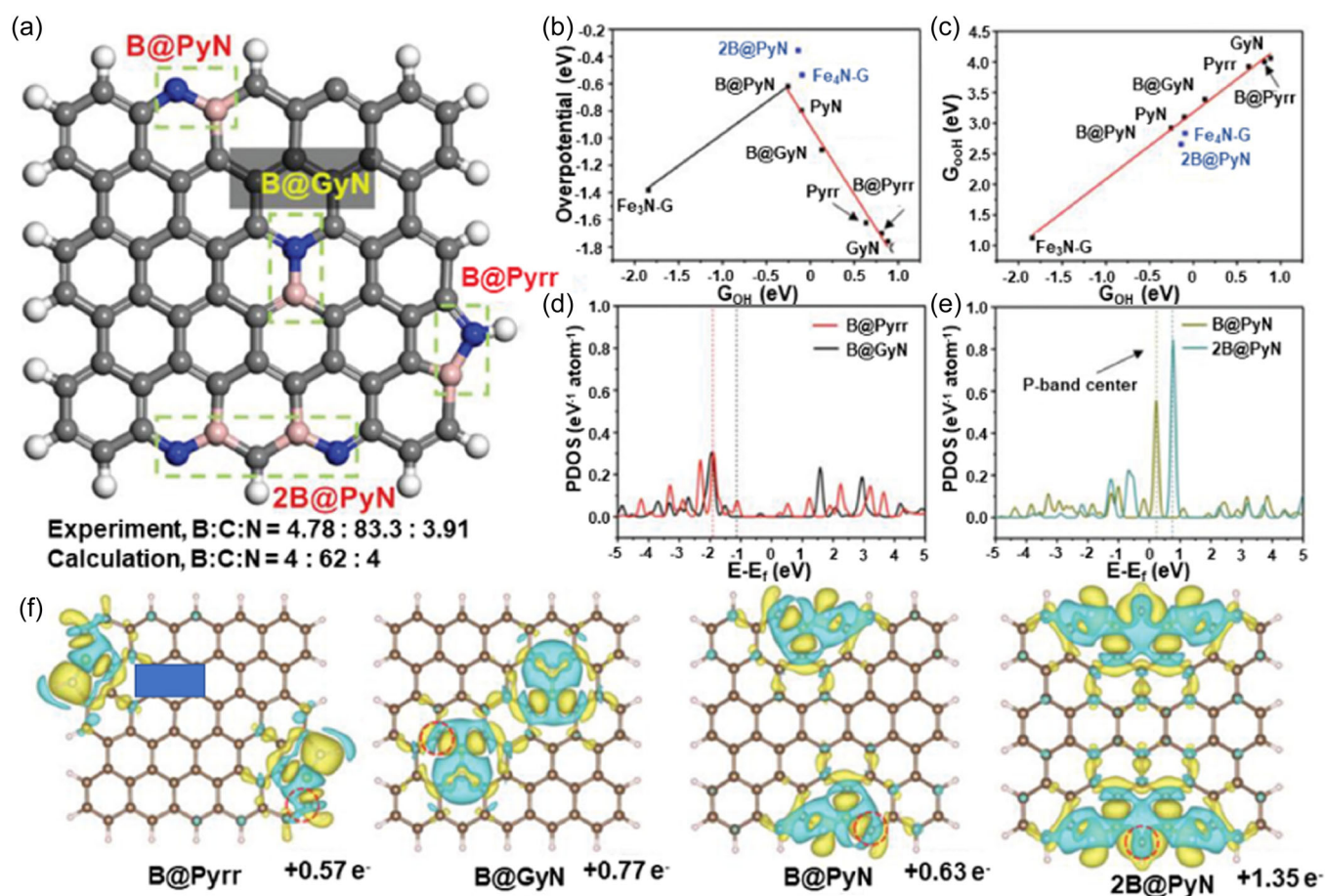


FIGURE 12 (a) N-B active sites structure model. (b and c) Volcano plot for N-B active sites. (d) The partial density of states for B@Pyrr and B@GyN. (e) The p-band center. (f) The charge density distribution for the B@Pyrr, B@GyN, B@PyN, and 2B@PyN. Reproduced with permission: Copyright 2022, Wiley-VCH.^[9]

theoretical study, the volcano plot of N, P coupled doping manifested the top position, indicating the minimum overpotentials. The N, P-coupled graphene model was deemed to be the active unit. The reaction process of N, P-coupled graphene was described through the designed model structure. The synergistic effects of NPMC material enhanced the ORR and OER activities. Meanwhile, Gao et al.^[129] reported a 3D S, N co-doped carbon material (PHC). Benefiting from the synergistic effect and 3D pore structures, the PHC catalyst revealed outstanding ORR activity and stability in alkaline electrolytes.

To figure out the catalytic mechanism of S, N co-doped, Zhu et al.^[91] prepared N/S doped porous carbon materials (CF-K-A) with defect-rich ultralight biomass scrap materials as N and S sources. As shown in Figure 13, the four structure models (pristine-G, defected-G, N-doped defected-G, and N/S-codoped defected-G) were designed and constructed using the DFT method. Moreover, the NS-D-G exhibited the strongest charge density, resulting in the local electron cloud change. When the charge density of carbon atoms

exceeded 0.15, the carbon atoms could be regarded as active units for ORR. DFT showed that the defect structure and N, S doped regulated the charge densities of the carbon skeleton. These unique characteristics provided abundant active sites. The CF-K-A1000 showed an excellent ORR activity.

In addition, Pang et al.^[130] designed N, S-codoped carbon material (NS@CFs). Tuning the N and S doping, the sample material achieved the best defect levels to boost the ORR activity. The N₁S₁@CF displayed a higher $E_{1/2}$ (0.88 V) than Pt/C catalysts (0.85 V). Apart from the codope of the heteroatom in the carbon matrix, the tri-doped material has also been investigated. Wang et al.^[99] prepared B, N, and F tri-doped carbon nanofibers (BNF-LCFs) through the electrospinning and annealing methods. Benefiting from the abundant defect sites and the B, N, and F tri-doped, the BNF-LCFs catalyst reflected an excellent bifunctional performance ($\Delta E = 0.728$ V). Moreover, The BNF-LCFs-based ZAB presented a high OCV (1.536 V) and satisfactory cycling properties. Wang et al.^[102] prepared tir-doped defect graphene (NSP-Gra) using the ball-milling and pyrolysis strategy. The abundant defect of graphene could improve the well-distributed of the heteroatoms. Thus, the NSP-Gra presented a good bifunctional activity ($\Delta E = 0.94$ V). Furthermore, the NSP-Gra-based ZAB exhibited a superior power density (225 mW cm^{-2}). In a word, reasonable doping or manufacturing defects in metal-free carbon materials is a good strategy to improve their ORR and OER catalytic activities. However, the multi-doping strategy can cause complex internal factors, which lead to the obfuscation of the catalytic mechanism.

3.2.2 | Carbon-based transition metal catalysts (CB-TMC)

TMC is mainly divided into transition metal oxide/sulfide/phosphide electrocatalysts and carbon composite transition metal electrocatalysts.^[131–133] In recent years, the preparation of CB-TMC has made great progress to further improve the catalytic property, owing to cost-effectiveness, abundant reserves, remarkable electrochemical activity, and excellent durability. Thus, recent advances in transition metal-based electrocatalysts will be the detailed description in this chapter. Moreover, recent advancements in CB-TMC toward electrocatalytic properties is listed in Table 4.

Transition metal oxides (TMOs) are deemed to the high OER catalytic activity due to the various and adjustable electronic structures. Thus, the TMOs have aroused great interest.^[145] However, most TMOs are semiconductor materials, resulting in low electron

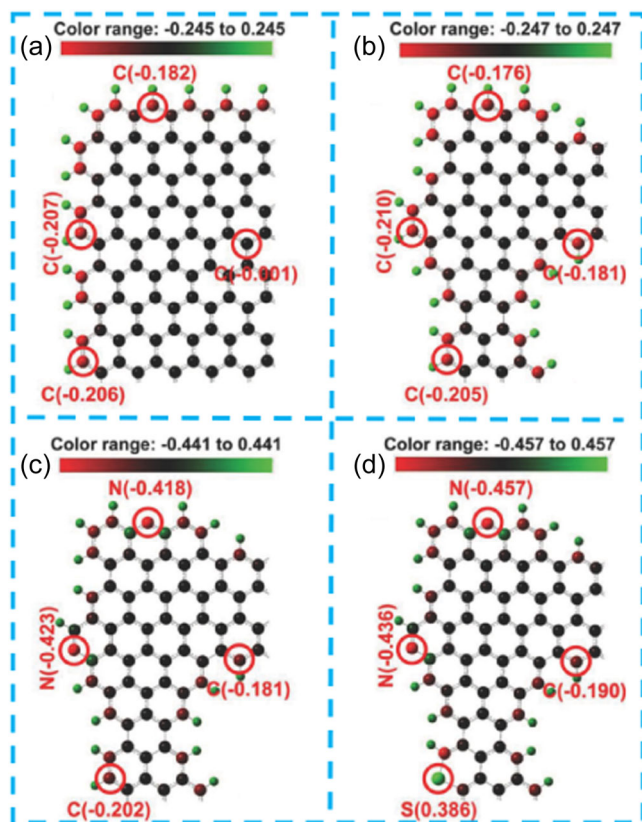


FIGURE 13 Charge density distribution of four graphene models. (a) Unmodified graphene. (b) Defective graphene. (c) Nitrogen-modified defective graphene. (d) Nitrogen/sulfur-modified defective graphene. Reproduced with permission: Copyright 2018, Wiley-VCH.^[91]

TABLE 4 Summary of recent advancement in TMBC.

Catalysts	$E_{1/2}$ vs. RHE (V)	Overpotential (mV)	Power density (mW cm ⁻²)	Cycling stability (x = h, y = mA cm ⁻²)
V-Co ₃ O ₄ ^[134]	0.82	351.0	120.3	1368 x at 5 y
Co ₃ O ₄ /N-rGO ^[135]	0.79	490.0	/	25 x at 3 y
N-Co ₃ O ₄ @NC ^[131]	0.77	266.0	174.1	50 x at 5 y
porous Ni/NiO ^[136]	0.75	260.0	225.0	120 x at 2 y
Co ₂ P/CoNPC ^[137]	0.84	326.0	116.0	60 x at 10 y
S-GNS/NiCo ₂ S ₄ ^[138]	0.88	330.0	216.3	100 x at 10 y
FeSNC-TA ^[139]	0.91	/	85.6	/
Fe-N ₂ O/G ^[140]	0.86	/	164.7	150 x at 20 y
P/Fe-N-C ^[141]	0.90	304.0	269.0	192 x at 10 y
FeN ₄ CB ^[142]	0.84	350.0	177.0	220 x at 10 y
S-COF@CNT ^[143]	0.77	/	158.7	600 x at 5 y
FeCo-MHs ^[144]	0.95	/	319.7	2000 x at 10 y
COP _{BTC} -Co ^[21]	0.86	390.0	157.7	100 x at 10 y
Co-CMS ^[13]	0.83	/	219.0	594 x at 2 y

Abbreviation: RHE, reversible hydrogen electrode.

mobility. When acting as the air cathode of ZABs, large electrochemical and ohmic polarization will occur. To solve the problem of poor conductivity, TMOs can usually optimize the electronic structure. Moreover, the TMOs can combine with conductive polymers or metal doping to form conductive networks, thus achieving excellent bifunctional catalysts. Rao et al.^[134] designed a mesoporous V-doped Co₃O₄ (V-Co₃O₄) material. The spinel-type Co₃O₄ was identified as a prospecting TMOs material, while the configuration of Co³⁺ exhibited the inefficient catalytic property. Therefore, the e_g occupancy of Co₃O₄ was needed to optimize. Thus, the V-Co₃O₄ catalyst possessed a desirable configuration (1.010), achieving the optimal binding strength for the rate-determining step of the ORR and OER process. The V-Co₃O₄ electrocatalyst was superior to the commercial Pt-IrO₂ catalysts. And, the V-Co₃O₄-based ZABs presented the specific capacity (814 mAhg_{zn}⁻¹). Liu et al.^[136] designed and regulated the interfacial electronic structure to form the charge density difference and improve electronic conductivity. The mesoporous Ni/NiO was prepared using hydrothermal and postacid etching. The Ni nanoparticles were introduced into the abundant pore structure to expose the active sites. Accordingly, the mesoporous Ni/NiO catalyst exhibited a remarkable bifunctional performance ($\Delta E = 0.75$ V). Furthermore, the mesoporous Ni/NiO-based ZAB possessed displayed

a large peak power density (225 mW cm⁻²). In addition, the TMOs combined with the carbon-based material was also an efficient method to enhance the electron transfer. Chen et al.^[146] synthesized a ultrathin mesoporous Co₃O₄ loaded on the carbon cloth (ultrathin Co₃O₄/CC). The ultrathin Co₃O₄/CC electrocatalyst possessed high ORR and OER activity due to the abundant active materials and porous structure. The ultrathin Co₃O₄/CC material as the air cathode showed outstanding rechargeable performance (voltage gap 0.92 V). In Figure 14a, Li et al.^[135] designed and prepared the hybrid nanosheet (Co₃O₄ nano-layers with N-rGO nanosheet). As shown in Figure 14b, HRTEM and SAED confirmed the structure of spinel Co₃O₄. Moreover, the lattice spacing was 0.243 and 0.285 nm respectively, which matched well with the (311) and (220) lattice plane of Co₃O₄. The N-rGO not only had excellent conductivity and a large specific surface area but also promoted the ORR and OER processes. Benefiting from the synergetic effect of Co₃O₄ and N-rGO nanosheet, the hybrid nanosheet has excellent ORR and OER performance ($\Delta E = 0.92$ V), which was superior to single component catalytic materials (N-rGO or Co₃O₄ nanosheets) in Figure 14c). Wang et al.^[131] constructed N-doped Co₃O₄ nanoparticles/N-doped carbon skeleton through using ZIF-67 with NH₃ in the pyrolysis (N-Co₃O₄@NC). DFT calculation showed that the N-doping could enhance the

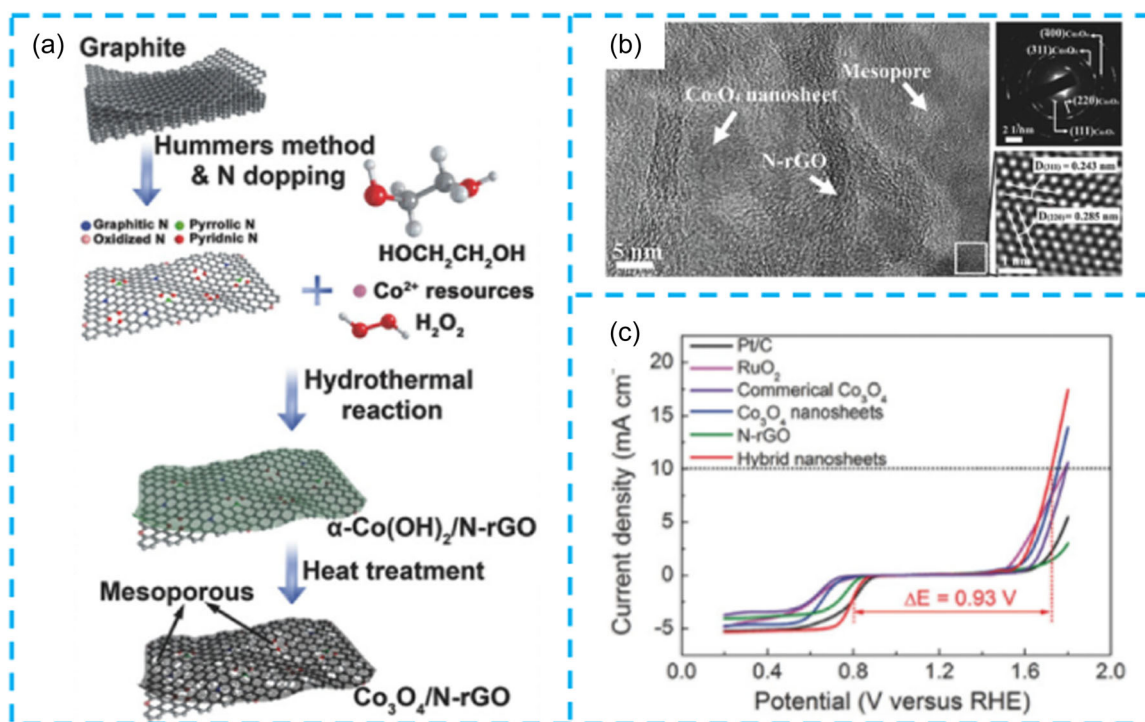


FIGURE 14 (a) Synthesis route of Co₃O₄/N-rGO hybrid nanosheet. (b) HRTEM and SAED of Co₃O₄/N-rGO hybrid nanosheets. (c) ORR and OER polarization curves of materials. Reproduced with permission: Copyright 2018, Wiley-VCH.^[135]

conductivity, accelerate the reaction kinetics, and optimize the adsorption energy of the rate-determining step, thereby promoting the electrocatalytic activity. Thus, the N-Co₃O₄@NC exhibited a low overpotential (266 mV) at 10 mA cm⁻² and Tafel slope (54.9 mV dec⁻¹). The N-Co₃O₄@NC as the air electrode also illustrated a prominent power density (174 mW cm⁻²) and high round-trip efficiency (58.6%).

The activity of transition metal sulfide (TMChs) electrocatalysts is comparable to or even better than that of traditional noble metal catalysts. TMChs have unique structural characteristics, high conductivity, and thermal stability, making them potential electrocatalysts.^[147] For example, M-sulfide (M = Ni, Co, and other metal), the sulfide atom on the catalyst surface will be oxidized and lost, generating the high OER activity substance (MOOH) during the catalytic process.

Chen et al.^[148] employed NiS nanosheets to grow on stainless steel (NiS@SLS). The strong adhesion between porous NiS nanosheets and stainless steel was constructed. Thus, the NiS@SLS catalyst possessed high electrical conductivity and abundant active sites. Therefore, the NiS@SLS displayed an outstanding OER activity at 11 mA cm⁻² (overpotential: 297 mV) and rapid reaction process (47 mV dec⁻¹). The bimetallic sulfides possessed higher conductivity and intrinsic activity than the conventional monometallic sulfides due to the synergistic influence

between bimetals. Xuan et al.^[149] synthesized porous NiFe-based sulfide (Ni-Fe-S) using hydrothermal reaction and annealing process (PBA). The Ni-Fe-S material had an abundant pore structure and composite phase (Fe₅Ni₄S₈ and NiS), which was conducive to rapid charge transfer and improved the stability of the material. In the OER process, the Ni-Fe-S_{3.1}-160 catalyst showed excellent OER electrocatalytic activity with a low overpotential of 200 mV at 10 mA cm⁻². Luan et al.^[150] designed a FeS-NiS hybrid nanosheet, which was grown on Ti mesh (FeS NiS/TM) via hydrothermal sulfuration. The electrochemical test showed that the FeS-NiS/TM had a very small overpotential of 260 mV at 10 mA cm⁻². Its excellent electrocatalytic activity was attributed to the synergistic effect of hybrid FeS and NiS. Liu et al.^[151] introduced Fe atom into MOF-derived NiCoS through a simple two-step hydrothermal method. According to DFT calculation, defect structures could cause more electrons in the near Fermi level, which was beneficial to electron transfer in the OER process. Based on the above description, the TMChs reflected the prominent OER performance while the ORR activity was deficient. To improve the ORR activity, the TMChs combined with carbon-based material to attain a bifunctional electrocatalyst. As shown in Figure 15a, Liu et al.^[138] prepared sea urchin-like NiCo₂S₄ composite, which was wrapped with S modificatory graphene nanosheets (S-GNS/NiCo₂S₄) through a simple hydrothermal reaction and sulfuration process. In

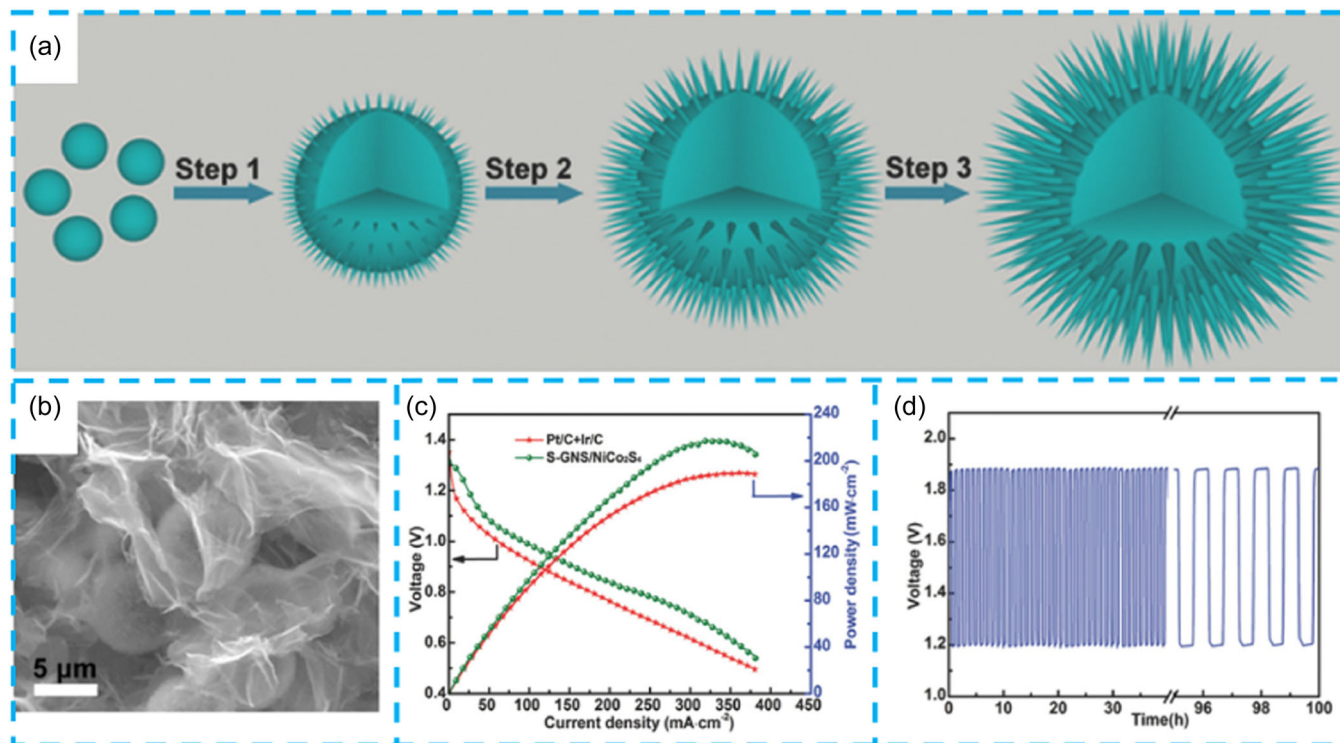


FIGURE 15 (a) Schematic diagram of the formation process for urchin-like carbonate hydroxide microspheres. (b) Polarization curves and corresponding power density curves. (c) ORR and OER curves of S-GNS/NiCo₂S₄ and other sample catalysts. (d) Galvanostatic charge/discharge test of the S-GNS/NiCo₂S₄ catalyst at 10 mA cm⁻². Reproduced with permission: Copyright 2018, Wiley-VCH.^[138]

Figure 15b, the NiCo₂S₄ was wrapped by sulfur-doped nanosheets. This work emphasized the role of each part for the composite S-GNS/NiCo₂S₄. Among them, NiCo₂S₄ had a unique hierarchical and mesoporous structure, which could provide a large number of catalytic active sites. Moreover, the NiCo₂S₄ part possessed multiple valences and high conductivity, thus markedly improving the OER activity. The S-GNS part could increase the ORR electrocatalytic activity due to the S-doped causing the reduction of binding energy for the ORR process. Benefiting from the synergistic effect of S-GNS and NiCo₂S₄, the S-GNS/NiCo₂S₄ composites had an excellent power density of 216.3 mW cm⁻² and cyclic life (Figure 15c,d) due to the existence of NiCo₂S₄ and S-GNS.

In addition, Lu et al.^[152] fabricated a FeCo-based S composite loaded on rGO (FeCo₈S₈ NS/rGO) using a colloidal strategy. According to DFT calculations, the appropriate Fe atom content in Co₉S₈ was crucial to the electrocatalytic activity. Moreover, the rGO part provided high conductivity and stability. Therefore, the FeCo₈S₈ NS/rGO composites exhibited a low ΔE (0.77 V). Moreover, the FeCo₈S₈ NS/rGO composites-based ZAB displayed a low voltage gap and negligible voltage loss for galvanostatic cycling at 10 mA cm⁻² (Figure 16d). In addition, Wang et al.^[153] constructed amorphous FeCo-NiS_x through the electrodeposition method. The DFT calculation manifested that the surface of FeCoNiS_x was

reconstructed to form unique tri-MOOH, which could boost OER activity. The restriction of the scaling relationship was broken due to the migration of oxygen intermediate. The tri-metallic S composite presented an outstanding OER activity (overpotential 202 mV) and rapid kinetic process (47 mV dec⁻¹).

Transition metal phosphides (TMPs) nanostructures are a class of important electrocatalysts, which have good conductivity, adjustable structure, and strong bonding ability with water molecules. The metal atoms in TMPs are partially positively charged (δ^+), while the P atoms retain the negative charge (δ^-). The special electronic structure is conducive to the adsorption of OH⁻ in the electrochemical reaction process, thereby promoting the progress of catalytic reactions. The multiphase structure is one of the promising energy storage and electrocatalytic active materials. Liu et al.^[154] synthesized hollow FeCo-P alloy composites through hydrothermal reaction (Fe-Co-P). The high-valent Fe could stabilize the low-valent Co, simulating the further enhancement of electrocatalytic activity and stability. The Fe-Co-P material possessed a low overpotential of 252 mV. For ZABs, the bi-function performance was necessary to meet the needs of large-scale commercial applications. For this reason, many strategies have been adopted to construct heterostructures and encapsulate them with a carbon matrix, which significantly improved the bifunctional activity of the

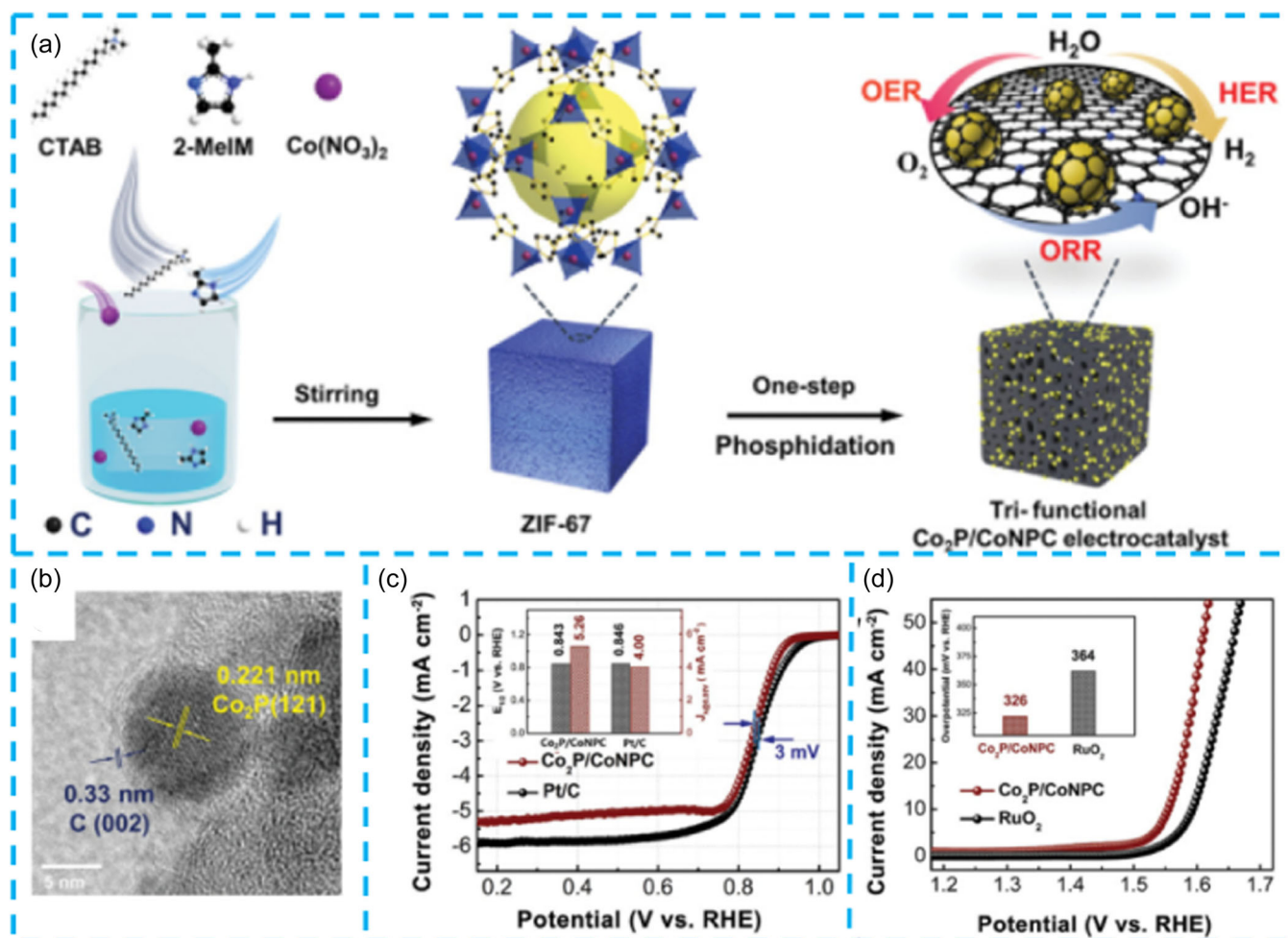


FIGURE 16 (a) Schematic diagram of Co₂P/CoNPC synthesis. (b) HRTEM image of Co₂P/CoNPC. (c) ORR polarization curves. (d) OER LSV curves. Reproduced with permission: Copyright 2020, Wiley-VCH.^[6]

required TMP nanostructures. Hou et al.^[133] made Co MOF nanosheets (Co MNS) grown on porous foam Ni, and then phosphatized to obtain porous foam nickel template carbon nanosheets with CoP_x nanoparticles insertion (CoP_x@CNS). The nitrogen-rich ligand of MOF restricted the in-situ growth of Co nanoparticles, endowing them with ultra-fine size (3–4 nm) and maintaining ultra-fine size in the subsequent phosphating process. The CoP_x@CNS material only needed the overpotential of 286 mV at 50 mA cm⁻², indicating that it had excellent catalytic activity for OER. In the process of electrocatalysis, the cobalt-P oxidation layers formed on the surface of CoP_x, which was the real catalytic site of OER. However, the ORR catalytic activity of CoP_x@CNS needed further improvement ($E_{1/2} = 0.76$ V).

Liu et al.^[137] prepared a Co₂P embedded in carbon matrix (Co₂P/CoNPC) using ZIF-67 as the precursor and red phosphorus as the curing agent in Figure 16a. As shown in Figure 16b, the Co₂P/CoNPC material displayed the obvious lattice space (0.221 nm), confirming the Co₂P crystal. Moreover, the carbon layer was covered

on the surface of Co₂P NP. DFT calculations demonstrated that the Co₂P exhibited a higher density near the Fermi level was higher than Co_nP (0 < n < 2), which was conducive to intermediate adsorption and charge transfer in the ORR/OER process. Benefiting from the synergistic effect between Co₂P and polyatomic modified carbon skeleton, Co₂P/CoNPC showed good bifunctional activity $\Delta E = 0.713$ V (Figure 16c,d).

Different from the catalyst mentioned above, the single atomic catalyst (SAC) has high atom utilization ($\approx 100\%$) and isolated metal atoms, which are uniformly dispersed on the carbon support.^[155] At present, SACs synthesis strategies are mainly divided into top-down and bottom-up. Most SACs are synthesized through a bottom-up strategy. The carbon material is adsorbed with metal ions and then is reduced to the metal atoms of a single distribution on the carbon carrier. In the process of preparing SACs, it is necessary to strictly control the amount of metal precursor. The high content of metal can cause the agglomeration of single

metal atoms, reducing atom utilization. Moreover, a large number of metal atoms are covered and become inactive, thus losing the active site.^[156] On the contrary, a small amount of metal in the precursor is also unable to obtain an optimum catalyst due to the unsaturated metal atom on the carbon support reducing the inherent catalytic activity. Therefore, it is important to optimize the metal precursor and their synthesis process. The top-down strategy employs the nanoparticles or smaller micron particles as precursors to transform into SACs under specific conditions. At present, the top-down strategy has been proven to be an efficient and feasible method to prepare homogeneous and well-defined SACs, including high-temperature pyrolysis, high-temperature atomic heat transfer, and so on. According to their composition and structure, they can be divided into transition metal salts adsorbed on organic polymer materials, metal-organic framework materials, and porphyrin-based polymer materials. To replace noble metal catalysts, SACs need to be continuously optimized to improve active sites and intrinsic activity.^[16]

To increase the intrinsic activity, the high capacity of atomically dispersed metal atoms is necessary. Organic polymer is a kind of high molecular weight compound which is composed of one or several structural units. The organic polymer has the advantages of high specific surface area, high conductivity, and flexible molecular structure design. In recent years, organic polymer materials have been used in gas/ion adsorption, catalysis, conductive materials, and many other fields. The atomic/molecule anchoring strategy uses the unsaturated coordination for the unique functional group material to anchor and capture TM atoms. Luo et al.^[157] fabricated the atomical Fe dispersion in the carbon matrix using a secondary atom-modified strategy in Figure 17a. The strategy could efficiently regulate the coordination environment of the Fe atoms, improving the reactive active center. Moreover, The synthetic Fe-N-C/N catalyst possessed the abundant Fe-N₅ configuration, which was the most effective ORR active site. As shown in Figure 17b, the monatomic Fe bright spots were observed on the carbon matrix. As revealed in Figure 17c,d, the Fe-N-C/FeN material had a significant electrocatalytic

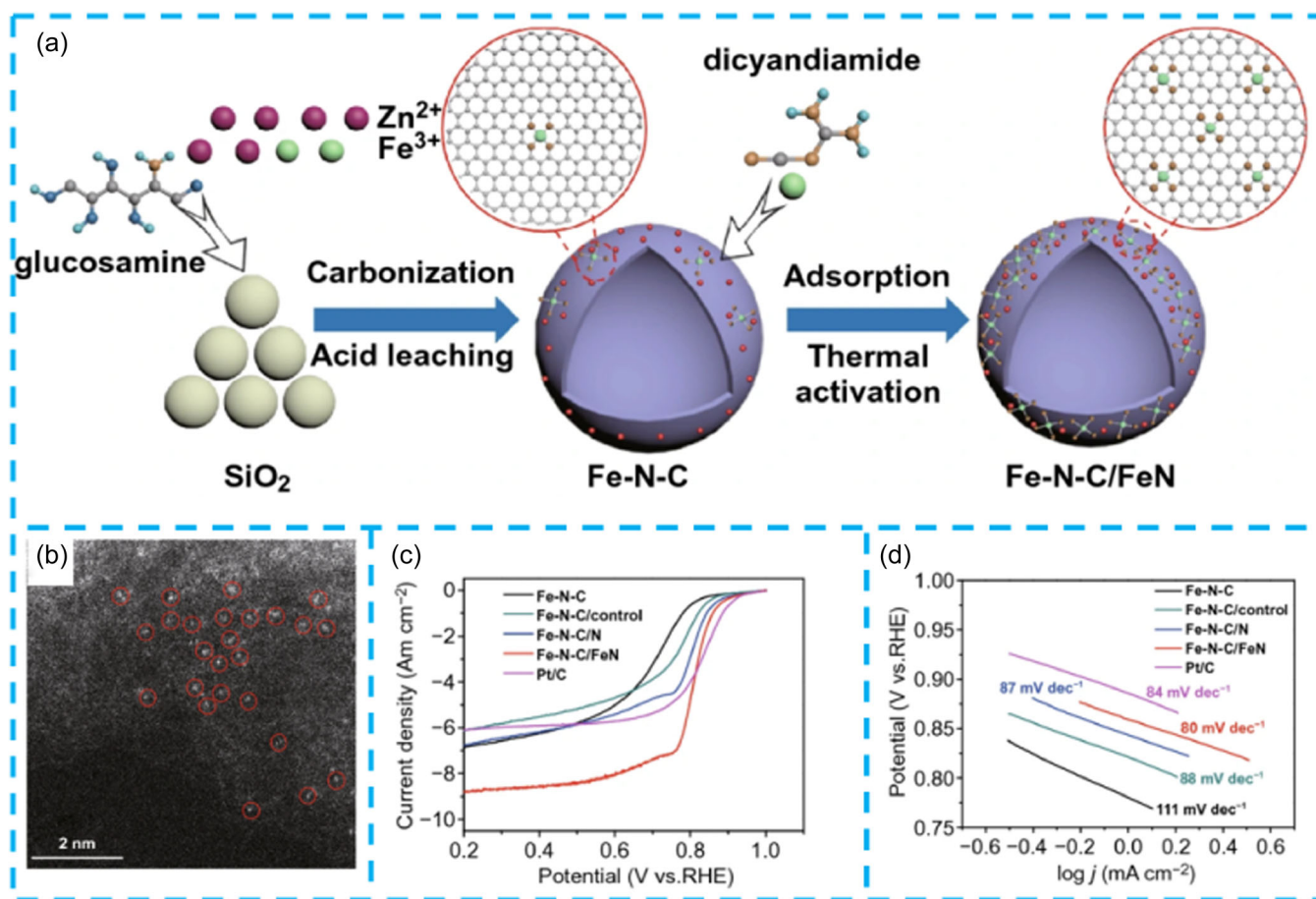


FIGURE 17 (a) Schematic diagram for Fe-N-C/FeN. (b) AC-STEM diagram of Fe-N-C/FeN. (c) Polarization and (d) Tafel slope curves of the synthetic sample and commercial Pt/C. Reproduced with permission: Copyright 2020, Springer Nature.^[157]

performance ($E_{\text{onset}} = 0.85 \text{ V}$, $E_{1/2} = 0.81 \text{ V}$) and a minimum tafel slope (80 mV dec^{-1}) in 0.1 M HClO_4 solution due to the porous structure and abundant Fe-N₅ active center. Zong et al.^[15] employed the alkali-activated carbon nanospheres method to create more adsorption and anchor sites for the metal atoms. The activated carbon nanospheres (CNS) had a large number of defect/vacancy structures and could selectively adsorb TM ions. Metal ions could be anchored to the CNS in a controlled manner. DFT confirmed that the N terminated vacancy was beneficial to anchors and restricted the Cu-As site. The synthesized TM-SAs@N-CNS showed excellent ORR electrocatalytic performance, especially Cu-SAs@N-CNs. Meanwhile, the Cu-SAs@N-CNs also exhibited obvious OER properties. Sarkar et al.^[12] put forward a special anchoring metal ions strategy. The method employed a small organic molecule (Ph-btpy) to bind Fe and Co atoms at its pyridinic N. The isolated two metals possessed a certain distance to prevent the metal atom agglomeration and then pyrolysis process generated the plentiful Fe-N_x/C and Co-N_x/C active center. The synthetic sample (Fe,Co,N-C) catalyst displayed a small $\Delta E = 0.74 \pm 0.02 \text{ V}$. The ZAB utilized Fe,Co,N-C catalysts as the air cathode exhibited an excellent power density (198.4 mW cm^{-2}). Xiang et al.^[158] carried out the Yamamoto reaction and synthesized a series of 2D covalent organic polymeric materials containing metals (C-COP-P-M), which precisely controlled the position of nitrogen atoms. In alkaline and acidic electrolytes, C-COP-P-M showed high efficiency $4e^-$ ORR process, good stability, and methanol resistance. To obtain the highly loaded single atom catalysts, several strategies have been reported such as confinement and coordination effect. These methods can control and limit transfer between metal and metal to effectively improve the metallic load content of the catalysts.

Metal-organic frameworks (MOFs) are composed of transition metal ions and organic ligands. MOFs are organic-inorganic hybrid materials with intramolecular cavities formed through self-assembly. MOFs as porous crystal materials have aroused great interest in many applications, such as ORR, OER, and CO₂ reduction,^[35] due to their ultrahigh specific surface area, high porosity diversity, and controllable chemical structure. In recent years, researchers have carried out in-depth research for MOF materials. The metal nodes of MOF materials are atomically dispersed and have obvious periodicity, and there is a certain distance between metal atoms. During carbonization, metal substances can be reduced to single metal atoms or metal clusters by the carbon of organic imidazoles. And metal single atoms and clusters are anchored on the porous carbon matrix.^[159] By reasonably designing the structure of MOFs, the metal-loaded

content can be raised. Meanwhile, the metal ligands can be prevented from agglomeration during the annealing process. Yin et al.^[160] designed a bimetallic Zn/Co MOFs material, and then annealing treatment (Co SAs/NC). The organic link chain was carbonized to reduce cobalt and zinc ligands at high temperatures. The Co single atoms were uniformly dispersed on N doped porous carbon matrix with metal high-loaded content over 4 wt%. Co SAs/NC catalyst (Co-N_x single sites) showed excellent ORR performance which was better than that of the Pt/C catalyst (0.811 V). Duan et al.^[161] loaded a nickel iron-based MOF (NiFe-MOF) array on foam nickel using a dissolution-crystallization mechanism. NiFe-MOF was made up of organic matter (2,6-naphthalenedicarboxyl) and inorganic matter (metal oxygen layer). The NiFe-MOF array has an ultra-thin plate structure (about 3.5 nm in thickness), high conductivity, and hierarchical porosity of foam nickel. After NiFe MOF was coated on the array of nickel foam, the NiFe-MOF array showed excellent electrocatalytic activity (overpotential 240 mV), fast reaction kinetics, and good durability. Wang et al.^[162] used an incompatible amino group as a Lewis base to stabilize Ru³⁺. The interaction between the lone pair electrons of the amino group and the d-electron orbital of Ru³⁺ confined Ru atoms in the carbon matrix and prevented the mutual aggregation of metal atoms. This process realized the introduction of Ru single atom and improved the atom utilization. For example, Liang et al.^[13] prepared a carbon molecular sieve (CMS) with highly ordered pore size and abundant -OH functional group in Figure 18a. The XPS spectrum of C1s and O1s shows two major peaks of 286.5 and 532.0 eV, corresponding to the C-O and -OH. (Figure 18b). The peaks at functional groups on CMS can be confirmed by ¹H magic angle spinning nuclear magnetic resonance (¹H MAS NMR). In Figure 18c, the strong resonance peaks at 2.20 and 0.75 ppm corresponded to C-OH groups. According to the specific experimental methods and theoretical calculations, the microporous structure and OH⁻ functional groups were conducive to the conversion of monoatomic catalysts. Benefiting from the highly dispersed metal single-atom and the unique porous structure, the Co-CMS material possessed a high $E_{1/2}$ (0.83 V) in Figure 18d. Moreover, the Co-CMS as the air cathode showed a low voltage gap (0.77 V) and high power density (219 mW cm^{-2}).

According to the above discussion, the anchoring mode of metal ions has changed from disorder to ordered qualification. The ordered and controllable qualification easier to raise the load content of metal single-atoms. However, the pyrolysis process is very energy-intensive. Meanwhile, the metal atoms reduce the surface free

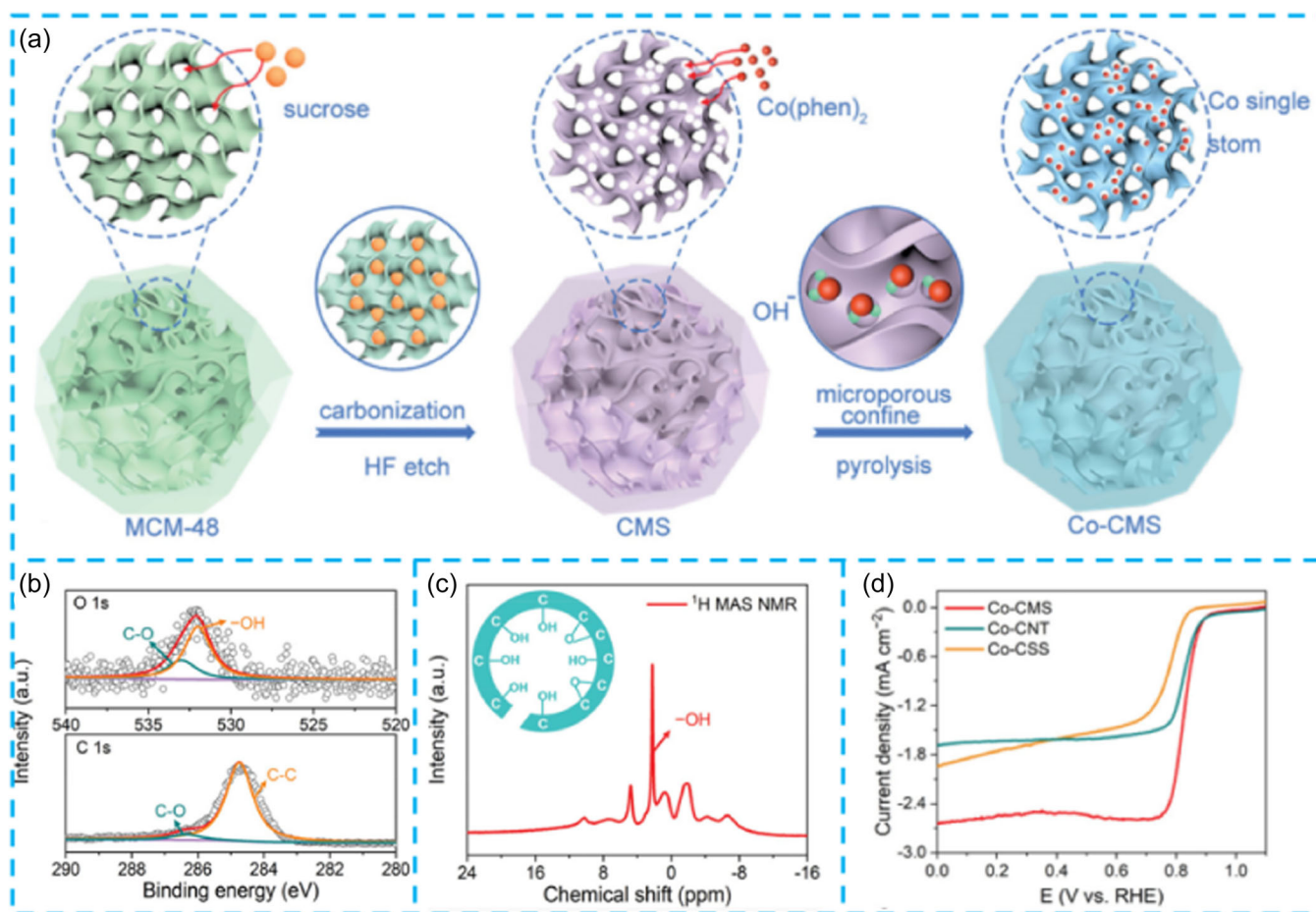


FIGURE 18 (a) Composite image of Co-CMS. (b) XPS spectra of High-resolution O 1s and C 1s in CMS. (c) ¹H MAS NMR spectrum of CMS. (d) LSV curve. Reproduced with permission: Copyright 2022, Wiley-VCH. CMS, carbon molecular sieve.^[13]

energy and are thermodynamically unstable during the pyrolysis process. The annealing treatment not only generates an abundant inactive structure but also reduces the efficient utilization of metal active sites. The simple catalytic system becomes complex and fuzzy making it challenging to achieve the precise active units. Therefore, the development of pyrolysis-free materials synthesis is a crucial adjective to realize the intrinsic quality of catalysts. The pyrolysis-free route can retain the original molecular structure, which elucidates structure–activity relationships and catalytic mechanisms for the optimum electrocatalysts.

3.2.3 | Molecular catalysts

Molecular materials are widely used in the study of catalytic mechanisms because of their clear molecular structure and strong designability. The construction of molecular catalysts can definitely solve the blurry structure units and. Molecular catalysts prepared

through polymerization of organic monomers. It maintain the original active site structure. Besides, molecular catalysts possess an unambiguous structure, which provide an advantage to investigate catalytic mechanism and performance optimization. The synthetic method can also significantly implement energy conservation. Compared to carbon-based material, the pyrolysis-free materials enhance the repeatability of material preparation, thereby providing definite model catalysts. Recently, well-defined porphyrin materials have been proposed. The porphyrin ring is a class of heterocyclic compounds connected by four pyrrole subunits and methylene bridge (=CH–), which can coordinate with metal ions.^[163] In nature, metalloporphyrin materials and their derivatives play a significant role in a variety of biological functions, such as electron transfer, oxygen (O₂) transport, activation, and many catalytic transformations. In plants, vitamin B12 is a Mg-porphyrin material that can absorb light for photosynthesis. In animals, heme is an iron-porphyrin material, which can carry and transport O₂ and CO₂. Inspired by the above,

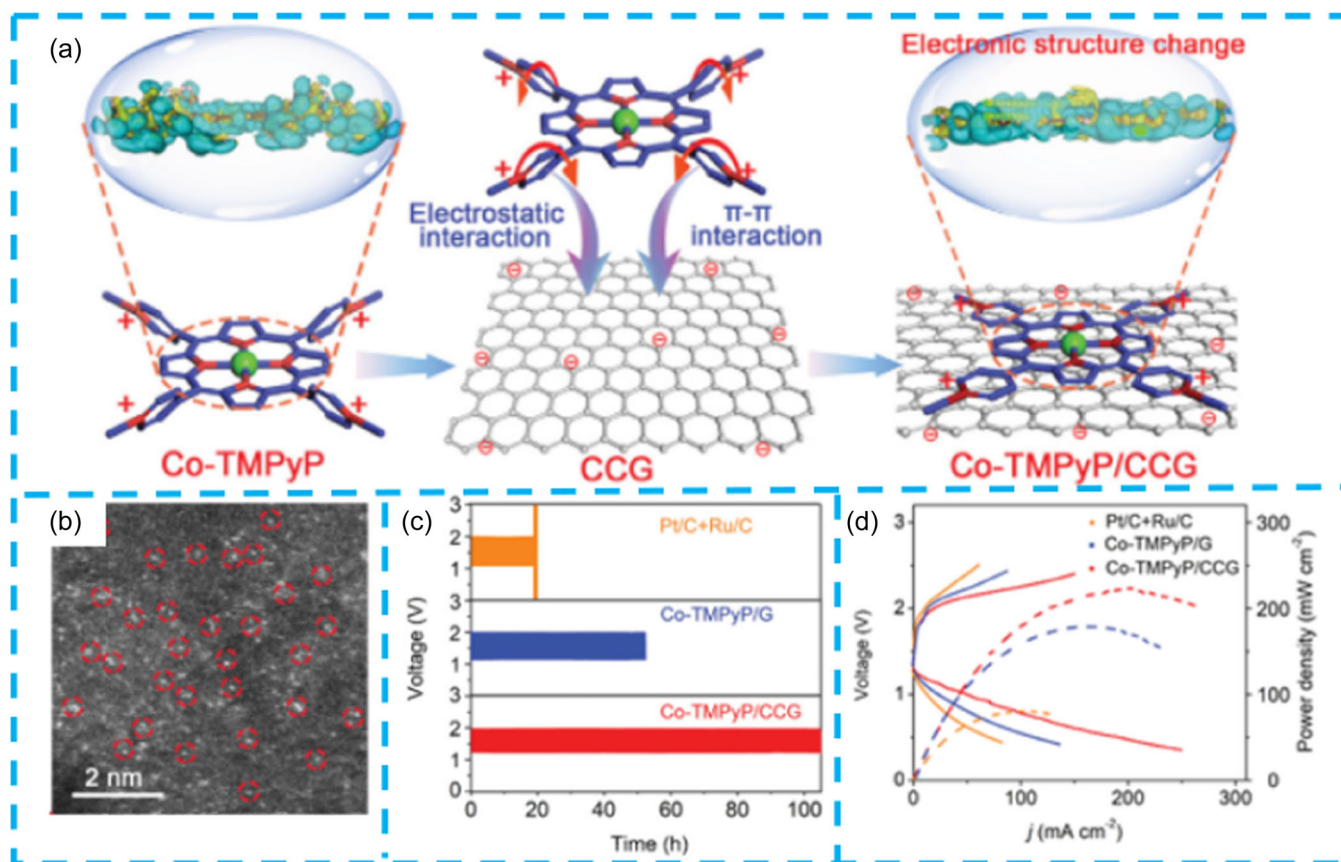


FIGURE 19 (a) Supermolecular assembly diagram of Co TMPyP/CCG. (b) HAADF-STEM image of the molecular catalyst. (c) Long-term cycle test of the material and Pt/C + Ru/C-based batteries at 2 mA cm^{-2} . (d) The polarization curve. Reproduced with permission: Copyright 2021, Wiley-VCH.^[19]

the porphyrin ring can combine metal (Fe, Co, Ni, Cu, Zn) ions to provide a rigid and stable coordination environment. The metalloporphyrin catalysts are stable in both acid and alkali electrolytic solutions.^[164] This unique stability feature provides feasibility for its practical application. At the same time, porphyrin molecules can be modified with different functional groups, thus making metalloporphyrins have different chemical and physical-chemical properties. Thus, the rational construction of the molecular structure is of great significance in exploring the catalytic mechanism and enhancing the bifunctional catalytic activity of metalloporphyrin materials. In the past decade, the rapid development of methodology and characterization technology caused the clear catalytic mechanism and structure-performance relationship. More and more molecular catalysts have been accurately designed to investigate the source of catalytic performance. For example, Peng et al.^[165] precisely designed and prepared SACs (*p*/SAC-Fe-X) through a pyrolysis-free route. The Fe-N-C moieties were formed by intermolecular interactions rather than the annealing process. DFT calculations

demonstrated that the graphene was attracted to Fe sites, making Fe-C an electronic channel. Moreover, the oxygen was only absorbed into the Fe units, suggesting the superior active sites. The *p*/SAC-Fe-X exhibited a prominent kinetic current density.

Mi et al.^[21] reported a well-defined network structure (COP_{BTC}-M) using a pyrolysis-free strategy. The COP_{BTC}-M possessed a symmetric charge configuration to alter the metal atom antibonding orbital. Therefore, the COP_{BTC}-M could testify to the catalytic active units. For theoretical prediction, the COP_{BTC}-M with MN₄₊₄ active center could balance bifunctional performance. Thus, COP_{BTC}-M displayed a superior $\Delta E = 0.76 \text{ V}$. Accordingly, the COP_{BTC}-M-based ZAB revealed a high power density and cycle stability. Zang et al.^[20] prepared a Fe-phthalocyanine framework (CPF-Fe). The CPF-Fe material and N-doped carbon were mixed to give CPF-Fe@NG. The catalyst had a high ORR performance ($E_{1/2} = 0.853 \text{ V}$) in acidic media. Cui et al.^[19] adsorbed Co(III)meso-tetra(N-methyl-4-pyridyl)porphyrin (Co-TMPyP) on chemically transformed graphene (CCG) through electrostatic adsorption and the π - π interactions, which shortened the Co-N coordination bond. Moreover, the

subtle regulation of conformation promoted electron transfer into the central metal ion. Figure 19a shows the synthesis route of Co-TMPyP/CCG. HAADF-STEM of Co-TMPyP/CCG displayed that there are a lot of bright spots in Figure 19b, corresponding to the Co single atoms dispersion. The Co-TMPyP/CCG catalysts had outstanding tri-functional properties. In Figure 19c,d, the Co-TMPyP/CCG-based ZAB showed outstanding specific capacity (793.0 mAh g^{-1}), long cycle life (100 h), and excellent power density (225.4 mW cm^{-2}).

Wan et al.^[166] investigated the degradation factors of FePc-based ORR activity in the acidic condition and then studied the full process of FePc-based material transformation by several characterization methods (Raman spectroscopy and mass spectrometry). The free radical was main factor, causing the instability of FePc. Moreover, the degradation mechanism possessed a high similarity between FePc-based and Fe-N-C catalysts. Li et al.^[167] precisely designed Fe-N configurations through diazonium methodology to understand the effect of Fe-Pyrrolic N_4 in ORR performance. The covalently functionalized Fe-Pyrrolic N_4 material exhibited higher activity density and excellent ORR activity. The preparation of optimum catalysts are urgently needed to study reaction mechanism. The evolution of molecular structure can be attained through operando measurement such as in situ technologies. Meanwhile, the theoretical calculation as good auxiliary method could also predict reaction pathways. Wang et al.^[168] constructed a novel Pyrazine-linked Fe-Pyrrole₄ (Pz-FeTPPr) material via polycondensation reaction and investigated ORR mechanism with in situ Raman measurements and DFT calculations. The evolution of Fe-N₄ site could be in-situ monitoring, demonstrating that the protonation of $^*\text{O}_2^-$ was the rate-determined step. The accelerated ORR kinetics was mainly attributed to proton-electron transfer step on $\text{D}_{\text{FePr}}\text{-A}_{\text{Pz}}$ modified Fe-N₄ site. Therefore, combining in situ characterization and theoretical prediction is of great importance for in-depth understanding between the structure-performance relationship.

4 | CONCLUSIONS AND OUTLOOKS

Compared with the extensive commercialization of LIBs, ZABs still face huge challenges in the practical application such as the carbonation and overflow of electrolyte, the hydrogen evolutional corrosion, dendrite growth as well as passivation of Zn anode, and the sluggish kinetics and high overpotential of the electrocatalysts. This review mainly describes the electrocatalytic evolution from fuzzy to unambiguous structure. Two categories including CB-MFM and CB-TMC have been selectively surveyed. The high

performance of carbon-based material can derive from defects, porous structure, heteroatom-doped, or other factors. The synergistic effects are defined as the origin of catalytic performance. Although the synergistic effect can improve the catalytic material activity, the direction of the destination (the best catalytic activity) is unclear. The precise active units can be beneficial to understanding the reaction principle and process for the catalyst. Currently, characterization techniques including AC-STEM, X-ray absorption near-edge structure (XANES), extended X-ray absorption fine structure (EXAFS), and so forth, have been used to study the electronic configuration and bonded structure of the catalyst materials. The internal structure of the catalyst will be further explored and investigated. Thus, the more subtle structure can be perceived and discussed to clearly distinguish the active centers of the catalysts. The well-defined SACs have been firmly believed clear model systems to probe the reactive mechanism for ORR and OER process at the atomic scale. Combined with theoretical simulation, the catalytic structure is constructed to open general direction and destination. The catalytic structure still needs to more explicit. The molecule catalysts just satisfy the structure clear and definite. Moreover, molecule catalysts retain uniform active units and devisable functional structures, which have directivity and purposiveness to design the best catalyst. Till now, the efficient synthesis approach needs more effort for the directed molecule catalysts. Meanwhile, the catalyst in the reaction process might undergo linkage structure changes. As a consequence, in situ characterization techniques are vital technology and then monitor the structure evolution of the active units, revealing the real catalytic theory. The catalytic performance can be further enhanced through the rational design of the catalytic structure. However, the high efficiency of molecule catalysts needs more striving to realize large production and practical application. The comprehensive overview will provide useful insights to a wide readership for the rational design catalyst. No doubt that the commercialization of ZABs is still a long way. With continued research efforts, the ZABs will bring commercial success in energy storage devices.

AUTHOR CONTRIBUTIONS

Wenhui Deng: Conceptualization; investigation; writing-original draft; writing—review and editing.
Mingjun Jing: Investigation; funding acquisition.
Tianjing Wu: Supervision; funding acquisition; review.
Wenzhang Li: Supervision; review. **Guoqiang Zou:** Supervision; review.

ACKNOWLEDGMENTS

This work was supported financially by the Distinguished Young Scholar Fund Project of Hunan Province Natural Science Foundation (2023JJ10041), the Hunan

Provincial Education Office Foundation of China (22A0114), the Science and Technology Program of Xiangtan (GX-ZD20211004, GX-ZD20221007), the Joint Funds of the National Natural Science Foundation of China (U20A20280), and Hunan Natural Science Foundation Joint Fund (2022JJ50136).

CONFLICT OF INTEREST STATEMENT

The authors declare no conflict of interest.

DATA AVAILABILITY STATEMENT

Data available within the article or its Supporting Information.

ORCID

Tianjing Wu  <http://orcid.org/0000-0003-1243-8440>

REFERENCES

- [1] S. Chu, A. Majumdar, *Nature* **2012**, 488, 294.
- [2] X. Liu, L. Dai, *Nat. Rev. Mater.* **2016**, 1, 16064.
- [3] Z. W. Seh, J. Kibsgaard, C. F. Dickens, I. Chorkendorff, J. K. Nørskov, T. F. Jaramillo, *Science* **2017**, 355, eaad4998.
- [4] F. Duffner, N. Kronemeyer, J. Tübke, J. Leker, M. Winter, R. Schmich, *Nat. Energy* **2021**, 6, 123.
- [5] Y. Li, H. Dai, *Chem. Soc. Rev.* **2014**, 43, 5257.
- [6] H. Liu, J. Guan, S. Yang, Y. Yu, R. Shao, Z. Zhang, M. Dou, F. Wang, Q. Xu, *Adv. Mater.* **2020**, 32, 2003649.
- [7] R. Paul, L. Zhu, H. Chen, J. Qu, L. Dai, *Adv. Mater.* **2019**, 31, e1806403.
- [8] Q. Zhai, Y. Pan, L. Dai, *Acc. Mater. Res.* **2021**, 2, 1239.
- [9] M. Fan, Q. Yuan, Y. Zhao, Z. Wang, A. Wang, Y. Liu, K. Sun, J. Wu, L. Wang, J. Jiang, *Adv. Mater.* **2022**, 34, e2107040.
- [10] Q. Wang, Y. Ji, Y. Lei, Y. Wang, Y. Wang, Y. Li, S. Wang, *ACS Energy Lett.* **2018**, 3, 1183.
- [11] K. Gong, F. Du, Z. Xia, M. Durstock, L. Dai, *Science* **2009**, 323, 760.
- [12] S. Sarkar, A. Biswas, E. E. Siddharthan, R. Thapa, R. S. Dey, *ACS Nano* **2022**, 16, 7890.
- [13] S. Liang, L. C. Zou, L. J. Zheng, F. Li, X. X. Wang, L. N. Song, J. J. Xu, *Adv. Energy Mater.* **2022**, 12, 2103097.
- [14] Y. Chen, S. Ji, C. Chen, Q. Peng, D. Wang, Y. Li, *Joule* **2018**, 2, 1242.
- [15] L. Zong, K. Fan, W. Wu, L. Cui, L. Zhang, B. Johannessen, D. Qi, H. Yin, Y. Wang, P. Liu, L. Wang, H. Zhao, *Adv. Funct. Mater.* **2021**, 31, 2104864.
- [16] W. Wan, C. A. Triana, J. Lan, J. Li, C. S. Allen, Y. Zhao, M. Iannuzzi, G. R. Patzke, *ACS Nano* **2020**, 14, 13279.
- [17] Y. Zang, D. Q. Lu, K. Wang, B. Li, P. Peng, Y. Q. Lan, S. Q. Zang, *Nat. Commun.* **2023**, 14, 1792.
- [18] Z.-Y. Wu, P. Zhu, D. A. Cullen, Y. Hu, Q.-Q. Yan, S.-C. Shen, F.-Y. Chen, H. Yu, M. Shakouri, J. D. Arregui-Mena, A. Ziabari, A. R. Paterson, H.-W. Liang, H. Wang, *Nat. Synth.* **2022**, 1, 658.
- [19] K. Cui, Q. Wang, Z. Bian, G. Wang, Y. Xu, *Adv. Energy Mater.* **2021**, 11, 2102062.
- [20] Y. Zang, C. Mi, R. Wang, H. Chen, P. Peng, Z. Xiang, S. Q. Zang, T. C. W. Mak, *Angew. Chem. Int. Ed.* **2021**, 60, 20865.
- [21] C. Mi, H. Yu, L. Han, L. Zhang, L. Zhai, X. Li, Y. Liu, Z. Xiang, *Adv. Funct. Mater.* **2023**, 33, 2303235.
- [22] Y. Arafat, M. R. Azhar, Y. Zhong, H. R. Abid, M. O. Tadé, Z. Shao, *Adv. Energy Mater.* **2021**, 11, 2100514.
- [23] X. Cai, L. Lai, J. Lin, Z. Shen, *Mater. Horiz.* **2017**, 4, 945.
- [24] Q. Wang, S. Kaushik, X. Xiao, Q. Xu, *Chem. Soc. Rev.* **2023**, 52, 6139.
- [25] C. Tang, H. F. Wang, X. Chen, B. Q. Li, T. Z. Hou, B. Zhang, Q. Zhang, M. M. Titirici, F. Wei, *Adv. Mater.* **2016**, 28, 6845.
- [26] X. Zhu, C. Hu, R. Amal, L. Dai, X. Lu, *Energy Environ. Sci.* **2020**, 13, 4536.
- [27] D. U. Lee, P. Xu, Z. P. Cano, A. G. Kashkooli, M. G. Park, Z. Chen, *J. Mater. Chem. A* **2016**, 4, 7107.
- [28] Y. Nie, L. Li, Z. Wei, *Chem. Soc. Rev.* **2015**, 44, 2168.
- [29] Z. L. Wang, D. Xu, J. J. Xu, X. B. Zhang, *Chem. Soc. Rev.* **2014**, 43, 7746.
- [30] J. Sun, N. Wang, Z. Qiu, L. Xing, L. Du, *Catalysts* **2022**, 12, 843.
- [31] J. Fu, Z. P. Cano, M. G. Park, A. Yu, M. Fowler, Z. Chen, *Adv. Mater.* **2017**, 29, 1604685.
- [32] Y.-J. Kim, K.-S. Ryu, *Appl. Surf. Sci.* **2019**, 480, 912.
- [33] S. J. Banik, R. Akolkar, *J. Electrochem. Soc.* **2013**, 160, D519.
- [34] M. Xu, D. G. Ivey, Z. Xie, W. Qu, *J. Power Sources* **2015**, 283, 358.
- [35] F. Cheng, J. Chen, *Chem. Soc. Rev.* **2012**, 41, 2172.
- [36] Y. Peng, C. Lai, M. Zhang, X. Liu, Y. Yin, Y. Li, Z. Wu, *J. Power Sources* **2022**, 526, 231173.
- [37] L. Zhang, B. Zhang, T. Zhang, T. Li, T. Shi, W. Li, T. Shen, X. Huang, J. Xu, X. Zhang, Z. Wang, Y. Hou, *Adv. Funct. Mater.* **2021**, 31, 2100186.
- [38] H. Kim, G. Jeong, Y.-U. Kim, J.-H. Kim, C.-M. Park, H.-J. Sohn, *Chem. Soc. Rev.* **2013**, 42, 9011.
- [39] Z. Zhao, J. Zhao, Z. Hu, J. Li, J. Li, Y. Zhang, C. Wang, G. Cui, *Energy Environ. Sci.* **2019**, 12, 1938.
- [40] S.-M. Lee, Y.-J. Kim, S.-W. Eom, N.-S. Choi, K.-W. Kim, S.-B. Cho, *J. Power Sources* **2013**, 227, 177.
- [41] Y. Shen, K. Kordesch, *J. Power Sources* **2000**, 87, 162.
- [42] A. Nakata, H. Arai, H. Murayama, K. Fukuda, T. Yamane, T. Hirai, Y. Uchimoto, J.-i Yamaki, Z. Ogumi, *APL Mater.* **2018**, 6, 047703.
- [43] Z. Ji-ling zhu, Z. Yun-Hong zhou, Y. Hanxi Yang, *J. Power Sources* **1997**, 69, 169.
- [44] D. Stock, S. Dongmo, F. Walther, J. Sann, J. Janek, D. Schröder, *ACS Appl. Mater. Interfaces* **2018**, 10, 8640.
- [45] Y. Zhou, J. Pan, X. Ou, Q. Liu, Y. Hu, W. Li, R. Wu, J. Wen, F. Yan, *Adv. Energy Mater.* **2021**, 11, 2102047.
- [46] S. Hosseini, S. J. Han, A. Arponwicanop, T. Yonezawa, S. Kheawhom, *Sci. Rep.* **2018**, 8, 11273.
- [47] S. Hosseini, A. Abbasi, L. O. Uginet, N. Hastraete, S. Praserttham, T. Yonezawa, S. Kheawhom, *Sci. Rep.* **2019**, 9, 14958.
- [48] H. Yang, *J. Power Sources* **2004**, 128, 97.
- [49] C. J. Lan, C. Y. Lee, T. S. Chin, *Electrochim. Acta* **2007**, 52, 5407.
- [50] G. D. Wilcox, P. J. Mitchell, *J. Power Sources* **1990**, 32, 31.
- [51] J. Zhu, Y. Zhou, *J. Power Sources* **1998**, 73, 266.

- [52] M.-C. Huang, S.-H. Huang, S.-C. Chiu, K.-L. Hsueh, W.-S. Chang, C.-C. Yang, C.-C. Wu, J.-C. Lin, *J. Chin. Chem. Soc.* **2018**, *65*, 1239.
- [53] H.-I. Kim, H.-C. Shin, *J. Alloys Compd.* **2015**, *645*, 7.
- [54] D. Schröder, N. N. Sinai Borker, M. König, U. Krewer, *J. Appl. Electrochem.* **2015**, *45*, 427.
- [55] P. K. Leung, C. Ponce-de-León, C. T. J. Low, F. C. Walsh, *Electrochim. Acta* **2011**, *56*, 6536.
- [56] Y. Wen, J. Cheng, L. Zhang, X. Yan, Y. Yang, *J. Power Sources* **2009**, *193*, 890.
- [57] A. R. Mainar, E. Iruin, L. C. Colmenares, J. A. Blázquez, H.-J. Grande, *Energy Sci. Eng.* **2018**, *6*, 174.
- [58] A. R. Mainar, O. Leonet, M. Bengoechea, I. Boyano, I. de Meatza, A. Kvasha, A. Guerfi, J. Alberto Blázquez, *Int. J. Energy Res.* **2016**, *40*, 1032.
- [59] D. M. See, R. E. White, *J. Chem. Eng.* **1997**, *42*, 1266.
- [60] C. W. Lee, K. Sathiyarayanan, S. W. Eom, H. S. Kim, M. S. Yun, *J. Power Sources* **2006**, *159*, 1474.
- [61] J. Lee, B. Hwang, M.-S. Park, K. Kim, *Electrochim. Acta* **2016**, *199*, 164.
- [62] Z. Cao, H. Hu, M. Wu, K. Tang, T. Jiang, *J. Mater. Chem. A* **2019**, *7*, 17581.
- [63] A. Li, A. Wang, J. Chen, *J. Appl. Polym. Sci.* **2004**, *92*, 1596.
- [64] J. Fu, J. Zhang, X. Song, H. Zarrin, X. Tian, J. Qiao, L. Rasen, K. Li, Z. Chen, *Energy Environ. Sci.* **2016**, *9*, 663.
- [65] M. Li, B. Liu, X. Fan, X. Liu, J. Liu, J. Ding, X. Han, Y. Deng, W. Hu, C. Zhong, *ACS Appl. Mater. Interfaces* **2019**, *11*, 28909.
- [66] G. M. Wu, S. J. Lin, C. C. Yang, *J. Membr. Sci.* **2006**, *280*, 802.
- [67] H. Miao, B. Chen, S. Li, X. Wu, Q. Wang, C. Zhang, Z. Sun, H. Li, *J. Power Sources* **2020**, *450*, 227653.
- [68] P. Zhang, K. Wang, Y. Zuo, M. Wei, H. Wang, Z. Chen, N. Shang, P. Pei, *ACS Appl. Mater. Interfaces* **2022**, *14*, 49109.
- [69] L. Li, F. Lu, C. Wang, F. Zhang, W. Liang, S. Kuga, Z. Dong, Y. Zhao, Y. Huang, M. Wu, *J. Mater. Chem. A* **2018**, *6*, 24468.
- [70] T. Lin, M. Shi, F. Huang, J. Peng, Q. Bai, J. Li, M. Zhai, *ACS Appl. Mater. Interfaces* **2018**, *10*, 29684.
- [71] X. Jin, G. Sun, G. Zhang, H. Yang, Y. Xiao, J. Gao, Z. Zhang, L. Qu, *Nano Res.* **2019**, *12*, 1199.
- [72] Z. Li, M. Li, Q. Fan, X. Qi, L. Qu, M. Tian, *ACS Appl. Mater. Interfaces* **2021**, *13*, 14778.
- [73] C. Liu, W. Xu, C. Mei, M. Li, W. Chen, S. Hong, W.-Y. Kim, S.-y. Lee, Q. Wu, *Adva. Energy Mater.* **2021**, *11*, 2003902.
- [74] R. Wang, M. Yao, S. Huang, J. Tian, Z. Niu, *Sci. China Mater.* **2022**, *65*, 2189.
- [75] P. Zhang, K. Wang, Y. Zuo, M. Wei, H. Wang, Z. Chen, N. Shang, P. Pei, *Chem. Eng. J.* **2023**, *451*, 138622.
- [76] T. N. T. Tran, H.-J. Chung, D. G. Ivey, *Electrochim. Acta* **2019**, *327*, 135021.
- [77] Z. Song, X. Liu, J. Ding, J. Liu, X. Han, Y. Deng, C. Zhong, W. Hu, *ACS Appl. Mater. Interfaces* **2022**, *14*, 49801.
- [78] Y. Guo, X. Zhou, Q. Tang, H. Bao, G. Wang, P. Saha, *J. Mater. Chem. A* **2016**, *4*, 8769.
- [79] L. Li, L. Liu, Y. Qing, Z. Zhang, N. Yan, Y. Wu, C. Tian, *Electrochim. Acta* **2018**, *270*, 302.
- [80] J. J. Xu, H. Ye, J. Huang, *Electrochem. Commun.* **2005**, *7*, 1309.
- [81] D. R. MacFarlane, N. Tachikawa, M. Forsyth, J. M. Pringle, P. C. Howlett, G. D. Elliott, J. H. Davis, M. Watanabe, P. Simon, C. A. Angell, *Energy Environ. Sci.* **2014**, *7*, 232.
- [82] M. Xu, D. G. Ivey, Z. Xie, W. Qu, E. Dy, *Electrochim. Acta* **2013**, *97*, 289.
- [83] T. J. Simons, D. R. MacFarlane, M. Forsyth, P. C. Howlett, *ChemElectroChem* **2014**, *1*, 1688.
- [84] H. Sadeghifar, N. Djilali, M. Bahrami, *J. Power Sources* **2014**, *248*, 632.
- [85] M. Wu, G. Zhang, M. Wu, J. Prakash, S. Sun, *Energy Storage Mater.* **2019**, *21*, 253.
- [86] X. Wang, X. Zhou, C. Li, H. Yao, C. Zhang, J. Zhou, R. Xu, L. Chu, H. Wang, M. Gu, H. Jiang, M. Huang, *Adv. Mater.* **2022**, *34*, e2204021.
- [87] F. Dong, M. Wu, Z. Chen, X. Liu, G. Zhang, J. Qiao, S. Sun, *Nano-Micro Lett.* **2021**, *14*, 36.
- [88] H. B. Yang, J. Miao, S.-F. Hung, J. Chen, H. B. Tao, X. Wang, L. Zhang, R. Chen, J. Gao, H. M. Chen, L. Dai, B. Liu, *Sci. Adv.* **2021**, *7*, e1501122.
- [89] T. V. Tam, S. G. Kang, M. H. Kim, S. G. Lee, S. H. Hur, J. S. Chung, W. M. Choi, *Adv. Energy Mater.* **2019**, *9*, 1900945.
- [90] T. Y. Ma, J. Ran, S. Dai, M. Jaroniec, S. Z. Qiao, *Angew. Chem. Int. Ed.* **2015**, *54*, 4646.
- [91] J. Zhu, W. Li, S. Li, J. Zhang, H. Zhou, C. Zhang, J. Zhang, S. Mu, *Small* **2018**, *14*, e1800563.
- [92] X. Zheng, J. Wu, X. Cao, J. Abbott, C. Jin, H. Wang, P. Strasser, R. Yang, X. Chen, G. Wu, *Appl. Catal. B* **2019**, *241*, 442.
- [93] J. Zhao, Q. Li, Q. Zhang, R. Liu, *Chem. Eng. J.* **2022**, *431*, 133730.
- [94] D. Xue, Y. Guo, B.-A. Lu, H. Xia, W. Yan, D. Xue, S. Mu, J.-N. Zhang, *Adv. Sci.* **2023**, *10*, 2302930.
- [95] F. Qiang, J. Feng, H. Wang, J. Yu, J. Shi, M. Huang, Z. Shi, S. Liu, P. Li, L. Dong, *ACS Catal.* **2022**, *12*, 4002.
- [96] X. Zhang, G. Han, S. Zhu, *Small* **2023**, *20*, 2305406.
- [97] S. Chen, L. Zhao, J. Ma, Y. Wang, L. Dai, J. Zhang, *Nano Energy* **2019**, *60*, 536.
- [98] C. Hu, L. Dai, *Adv. Mater.* **2017**, *29*, 1604942.
- [99] Y. Wang, R. Gan, S. Zhao, W. Ma, X. Zhang, Y. Song, C. Ma, J. Shi, *Appl. Surf. Sci.* **2022**, *598*, 153891.
- [100] J. Zhang, Z. Zhao, Z. Xia, L. Dai, *Nat. Nanotechnol.* **2015**, *10*, 444.
- [101] Z. Li, S. Ji, H. Liu, C. Xu, C. Guo, X. Lu, H. Sun, S. Dou, S. Xin, J. H. Horton, C. He, *Adv. Funct. Mater.* **2024**, *34*, 2314444.
- [102] Y. Wang, N. Xu, R. He, L. Peng, D. Cai, J. Qiao, *Appl. Catal. B* **2021**, *285*, 119811.
- [103] T. Lu, X. Hu, J. He, R. Li, J. Gao, Q. Lv, Z. Yang, S. Cui, C. Huang, *Nano Energy* **2021**, *85*, 106024.
- [104] X. Wang, R. K. M. Raghupathy, C. J. Querebillo, Z. Liao, D. Li, K. Lin, M. Hantusch, Z. Sofer, B. Li, E. Zschech, I. M. Weidinger, T. D. Kühne, H. Mirhosseini, M. Yu, X. Feng, *Adv. Mater.* **2021**, *33*, 2008752.
- [105] Z. Wu, Y. Yu, G. Zhang, Y. Zhang, R. Guo, L. Li, Y. Zhao, Z. Wang, Y. Shen, G. Shao, *Adv. Sci.* **2022**, *9*, 2200614.
- [106] Q. Liu, Y. Wang, L. Dai, J. Yao, *Adv. Mater.* **2016**, *28*, 3000.
- [107] L. Yan, Y. Xu, P. Chen, S. Zhang, H. Jiang, L. Yang, Y. Wang, L. Zhang, J. Shen, X. Zhao, L. Wang, *Adv. Mater.* **2020**, *32*, 2003313.
- [108] X. Zou, M. Tang, Q. Lu, Y. Wang, Z. Shao, L. An, *Energy Environ. Sci.* **2024**, *17*, 386.

- [109] Y. Jiao, Y. Zheng, K. Davey, S.-Z. Qiao, *Nat. Energy* **2016**, *1*, 16130.
- [110] J. Su, X. Cao, J. Wu, C. Jin, J.-H. Tian, R. Yang, *RSC Adv.* **2016**, *6*, 24728.
- [111] R. Langer, P. Błoński, C. Hofer, P. Lazar, K. Mustonen, J. C. Meyer, T. Susi, M. Otyepka, *ACS Appl. Mater. Interfaces* **2020**, *12*, 34074.
- [112] C. Zhang, N. Mahmood, H. Yin, F. Liu, Y. Hou, *Adv. Mater.* **2013**, *25*, 4932.
- [113] X. Zhang, Z. Lu, Z. Fu, Y. Tang, D. Ma, Z. Yang, *J. Power Sources* **2015**, 276, 222.
- [114] N. Yang, X. Zheng, L. Li, J. Li, Z. Wei, *J. Phys. Chem. C* **2017**, *121*, 19321.
- [115] Z. Yang, Z. Yao, G. Li, G. Fang, H. Nie, Z. Liu, X. Zhou, X. Chen, S. Huang, *ACS Nano* **2012**, *6*, 205.
- [116] L. Zhang, Z. Xia, *J. Phys. Chem. C* **2011**, *115*, 11170.
- [117] L. Zhang, J. Niu, M. Li, Z. Xia, *J. Phys. Chem. C* **2014**, *118*, 3545.
- [118] Z. Lu, S. Li, C. Liu, C. He, X. Yang, D. Ma, G. Xu, Z. Yang, *RSC Adv.* **2017**, *7*, 20398.
- [119] L. Li, Z. Wu, J. Zhang, Y. Zhao, G. Shao, *ChemElectroChem* **2021**, *8*, 4790.
- [120] C. Zhao, G. Liu, N. Sun, X. Zhang, G. Wang, Y. Zhang, H. Zhang, H. Zhao, *Chem. Eng. J.* **2018**, 334, 1270.
- [121] J. Gao, Y. Wang, H. Wu, X. Liu, L. Wang, Q. Yu, A. Li, H. Wang, C. Song, Z. Gao, M. Peng, M. Zhang, N. Ma, J. Wang, W. Zhou, G. Wang, Z. Yin, D. Ma, *Angew. Chem. Int. Ed.* **2019**, *58*, 15089.
- [122] J. Zhang, Y. Sun, J. Zhu, Z. Kou, P. Hu, L. Liu, S. Li, S. Mu, Y. Huang, *Nano Energy* **2018**, *52*, 307.
- [123] Q. Wang, Y. Lei, Y. Zhu, H. Wang, J. Feng, G. Ma, Y. Wang, Y. Li, B. Nan, Q. Feng, Z. Lu, H. Yu, *ACS Appl. Mater. Interfaces* **2018**, *10*, 29448.
- [124] T. Zhou, Y. Zhou, R. Ma, Z. Zhou, G. Liu, Q. Liu, Y. Zhu, J. Wang, *Carbon* **2017**, *114*, 177.
- [125] Q. Lv, N. Wang, W. Si, Z. Hou, X. Li, X. Wang, F. Zhao, Z. Yang, Y. Zhang, C. Huang, *Appl. Catal. B* **2020**, 261, 118234.
- [126] H. Fei, R. Ye, G. Ye, Y. Gong, Z. Peng, X. Fan, E. L. G. Samuel, P. M. Ajayan, J. M. Tour, *ACS Nano* **2014**, *8*, 10837.
- [127] R. Zhao, Q. Li, Z. Chen, V. Jose, X. Jiang, G. Fu, J.-M. Lee, S. Huang, *Carbon* **2020**, 164, 398.
- [128] Y. Zheng, Y. Jiao, L. Ge, M. Jaroniec, S. Z. Qiao, *Angew. Chem. Int. Ed.* **2013**, *52*, 3110.
- [129] S. Gao, H. Liu, K. Geng, X. Wei, *Nano Energy* **2015**, *12*, 785.
- [130] H. Pang, M. Wang, P. Sun, W. Zhang, D. Wang, R. Zhang, L. Qiao, W. Wang, M. Gao, Y. Li, J. Chen, K. Liang, B. Kong, *NPG Asia Mater.* **2023**, *15*, 15.
- [131] Z. Wang, W. Xu, X. Chen, Y. Peng, Y. Song, C. Lv, H. Liu, J. Sun, D. Yuan, X. Li, X. Guo, D. Yang, L. Zhang, *Adv. Funct. Mater.* **2019**, *29*, 1902875.
- [132] X. Shi, X. Ling, L. Li, C. Zhong, Y. Deng, X. Han, W. Hu, *J. Mater. Chem. A* **2019**, *7*, 23787.
- [133] C. C. Hou, L. Zou, Y. Wang, Q. Xu, *Angew. Chem. Int. Ed.* **2020**, *59*, 21360.
- [134] Y. Rao, S. Chen, Q. Yue, Y. Kang, *ACS Catal.* **2021**, *11*, 8097.
- [135] Y. Li, C. Zhong, J. Liu, X. Zeng, S. Qu, X. Han, Y. Deng, W. Hu, J. Lu, *Adv. Mater.* **2018**, *30*, 1703657.
- [136] P. Liu, J. Ran, B. Xia, S. Xi, D. Gao, J. Wang, *Nano-Micro Lett.* **2020**, *12*, 68.
- [137] H. Liu, J. Guan, S. Yang, Y. Yu, R. Shao, Z. Zhang, M. Dou, F. Wang, Q. Xu, *Adv. Mater.* **2020**, *32*, 2003649.
- [138] W. Liu, J. Zhang, Z. Bai, G. Jiang, M. Li, K. Feng, L. Yang, Y. Ding, T. Yu, Z. Chen, A. Yu, *Adv. Funct. Mater.* **2018**, *28*, 1706675.
- [139] H. Liu, L. Jiang, Y. Sun, J. Khan, B. Feng, J. Xiao, H. Zhang, H. Xie, L. Li, S. Wang, L. Han, *Adv. Funct. Mater.* **2023**, *33*, 2304074.
- [140] Y. Li, Y. Ding, B. Zhang, Y. Huang, H. Qi, P. Das, L. Zhang, X. Wang, Z.-S. Wu, X. Bao, *Energy Environ. Sci.* **2023**, *16*, 2629.
- [141] Y. Zhou, R. Lu, X. Tao, Z. Qiu, G. Chen, J. Yang, Y. Zhao, X. Feng, K. Müllen, *J. Am. Chem. Soc.* **2023**, *145*, 3647.
- [142] X. Zhao, X. Li, Z. Bi, Y. Wang, H. Zhang, X. Zhou, Q. Wang, Y. Zhou, H. Wang, G. Hu, *J. Energy Chem.* **2022**, *66*, 514.
- [143] Z.-y Mei, G. Zhao, C. Xia, S. Cai, Q. Jing, X. Sheng, H. Wang, X. Zou, L. Wang, H. Guo, B. Y. Xia, *Angew. Chem. Int. Edit.* **2023**, *62*, 202303871.
- [144] C. Chen, Y. Li, A. Huang, X. Liu, J. Li, Y. Zhang, Z. Chen, Z. Zhuang, Y. Wu, W.-C. Cheong, X. Tan, K. Sun, Z. Xu, D. Liu, Z. Wang, K. Zhou, C. Chen, *J. Am. Chem. Soc.* **2023**, *145*, 21273.
- [145] H. Osgood, S. V. Devaguptapu, H. Xu, J. Cho, G. Wu, *Nano Today* **2016**, *11*, 601.
- [146] X. Chen, B. Liu, C. Zhong, Z. Liu, J. Liu, L. Ma, Y. Deng, X. Han, T. Wu, W. Hu, J. Lu, *Adv. Energy Mater.* **2017**, *7*, 1700779.
- [147] Z. Zhang, X. Wang, G. Cui, A. Zhang, X. Zhou, H. Xu, L. Gu, *Nanoscale* **2014**, *6*, 3540.
- [148] J. S. Chen, J. Ren, M. Shalom, T. Feller, M. Antonietti, *ACS Appl. Mater. Interfaces* **2016**, *8*, 5509.
- [149] C. Xuan, W. Lei, J. Wang, T. Zhao, C. Lai, Y. Zhu, Y. Sun, D. Wang, *J. Mater. Chem. A* **2019**, *7*, 12350.
- [150] X. Luan, H. Du, Y. Kong, F. Qu, L. Lu, *Chem. Commun.* **2019**, 55, 7335.
- [151] R. Liu, S. Xu, X. Shao, Y. Wen, X. Shi, L. Huang, M. Hong, J. Hu, Z. Yang, *ACS Appl. Mater. Interfaces* **2021**, *13*, 47717.
- [152] S. Lu, J. Jiang, H. Yang, Y. J. Zhang, D. N. Pei, J. J. Chen, Y. Yu, *ACS Nano* **2020**, *14*, 10438.
- [153] A. Wang, X. Zhang, S. Gao, C. Zhao, S. Kuang, S. Lu, J. Niu, G. Wang, W. Li, D. Chen, H. Zhang, X. Zhou, S. Zhang, B. Zhang, W. Wang, *Adv. Mater.* **2022**, *34*, e2204247.
- [154] K. Liu, C. Zhang, Y. Sun, G. Zhang, X. Shen, F. Zou, H. Zhang, Z. Wu, E. C. Wegener, C. J. Taubert, J. T. Miller, Z. Peng, Y. Zhu, *ACS Nano* **2018**, *12*, 158.
- [155] J. Han, H. Bao, J.-Q. Wang, L. Zheng, S. Sun, Z. L. Wang, C. Sun, *Appl. Catal. B* **2021**, 280, 119411.
- [156] J. Ban, X. Wen, H. Xu, Z. Wang, X. Liu, G. Cao, G. Shao, J. Hu, *Adv. Funct. Mater.* **2021**, *31*, 2010472.
- [157] X. Luo, X. Wei, H. Wang, W. Gu, T. Kaneko, Y. Yoshida, X. Zhao, C. Zhu, *Nano-Micro Lett.* **2020**, *12*, 163.
- [158] Z. Xiang, Y. Xue, D. Cao, L. Huang, J. F. Chen, L. Dai, *Angew. Chem. Int. Ed.* **2014**, *53*, 2433.
- [159] B. Zhang, Y. Zheng, T. Ma, C. Yang, Y. Peng, Z. Zhou, M. Zhou, S. Li, Y. Wang, C. Cheng, *Adv. Mater.* **2021**, *33*, e2006042.
- [160] P. Yin, T. Yao, Y. Wu, L. Zheng, Y. Lin, W. Liu, H. Ju, J. Zhu, X. Hong, Z. Deng, G. Zhou, S. Wei, Y. Li, *Angew. Chem. Int. Ed.* **2016**, *55*, 10800.

- [161] J. Duan, S. Chen, C. Zhao, *Nat. Commun.* **2017**, 8, 15341.
- [162] X. Wang, W. Chen, L. Zhang, T. Yao, W. Liu, Y. Lin, H. Ju, J. Dong, L. Zheng, W. Yan, X. Zheng, Z. Li, X. Wang, J. Yang, D. He, Y. Wang, Z. Deng, Y. Wu, Y. Li, *J. Am. Chem. Soc.* **2017**, 139, 9419.
- [163] Z. Liang, H. Y. Wang, H. Zheng, W. Zhang, R. Cao, *Chem. Soc. Rev.* **2021**, 50, 2540.
- [164] J. Gu, Y. Peng, T. Zhou, J. Ma, H. Pang, Y. Yamauchi, *Nano Res. Energy* **2022**, 1, e9120009.
- [165] B. Z. Peng, L. V. Bock, R. Belardinelli, F. Peske, H. Grubmüller, M. V. Rodnina, *Sci. Adv.* **2019**, 5, eaaw2322.
- [166] L. Wan, K. Zhao, Y.-C. Wang, N. Wei, P. Zhang, J. Yuan, Z. Zhou, S.-G. Sun, *ACS Catal.* **2022**, 12, 11097.
- [167] Q. Li, Y. Xu, A. Pedersen, M. Wang, M. Zhang, J. Feng, H. Luo, M.-M. Titirici, C. R. Jones, *Adv. Funct. Mater.* **2023**, 33, 2311086.
- [168] Y. Wang, M. Wang, T. Chen, W. Yu, H. Liu, H. Cheng, W. Bi, M. Zhou, Y. Xie, C. Wu, *Angew. Chem. Int. Ed.* **2023**, 62, e202308070.

AUTHOR BIOGRAPHIES



Wenhui Deng is currently a doctoral student at Central South University. His research interests are on the atomic level design and mechanism understanding of active sites for electrocatalyst.



Tianjing Wu is an associate professor at School of Chemistry, Xiangtan University. He received his PhD at Central South University in 2019. His current research interests are the design, preparation and application of organic

electrode materials for advanced battery systems. He has published more than 30 peer-reviewed papers, granted with over 10 Chinese patents, and is the gainer of Hunan Outstanding Youth Fund.



Wenzhang Li received his BS degree and PhD degree from Central South University, both in physical chemistry of metallurgy. He joined the faculty of Central South University in January of 2012, where he is currently an associate professor in physical chemistry of metallurgy. His current research focuses on the design of inorganic nanomaterials, electrochemical and photoelectrochemical devices.



Guoqiang Zou is a professor at College of Chemistry and Chemical Engineering in Central South University. His current research is specializing in the advanced battery materials. He has published more than 60 peer-reviewed papers, granted with over 40 Chinese patents, and is the gainer of Hunan Outstanding Youth Fund. He is a young editorial board member of Nano-Micro Letters, Carbon Energy, Review Editor of Frontiers in Chemistry and Guest Editor of Nanomaterials.

How to cite this article: W. Deng, M. Jing, T. Wu, W. Li, G. Zou, *Carbon Neutralization* **2024**, 1. <https://doi.org/10.1002/cnl2.133>